Layered gabbros and peridotites from Piton des Neiges volcano, La Réunion Island

Carole Berthod, Laurent Michon, V. Famin, B. Welsch, Patrick Bachèlery, Jérôme Bascou

Layered gabbros and peridotites from Piton des Neiges volcano, La Réunion Island

C. Berthod[1,2,3*], L. Michon[2,3], V. Famin[2,3], B. Welsch[4], P. Bachèlery[1], J. Bascou[5]

[1]Université Clermont Auvergne, CNRS, IRD, OPGC, Laboratoire Magmas et Volcans, 6 avenue Blaise Pascal, 63178 Aubière, France.

[2] Université de La Réunion, Laboratoire GéoSciences Réunion, F-97744 Saint Denis, France.

[3] Université de Paris, Institut de physique du globe de Paris, CNRS, F-75005 Paris, France.

[4] University of Hawaii–Manoa, Department of Earth Sciences, 1680 East-West Road 96822 Honolulu, Hawaii, USA.

[5] Université de Lyon, Université Jean Monnet and UMR-CNRS 6524, Laboratoire Magmas et Volcans, 42023 Saint-Etienne, France

*Corresponding author: carole.berthod@uca.fr;

C. Berthod 0000-0001-6890-5541
L. Michon 0000-0002-4486-5378
V. Famin 0000-0001-7451-5363
B. Welsch
P. Bachèlery 0000-0002-0108-5486
J. Bascou 0000-0002-9357-6951

Highlights

- Layered gabbros and peridotites outcrop in the cirque of Salazie (Piton des Neiges).
- Plutonic rocks are parts of a large composite plutonic complex.
- Peridotitic and gabbroic bodies were active at different periods of time.
- Plutonic bodies were made by incremental stacking of independent magma intrusions.
- The proto summit of Piton des Neiges was located north of its current position

Keywords: La Réunion, Piton des Neiges, shield volcano, plutonic complex, layered intrusion, gabbro, peridotite.

ABSTRACT

We conducted a petrological study of the layered gabbros and peridotites outcropping in the cirque of Salazie, combining field investigations, geochemistry, petrography and, mineralogy to constrain the magmatic evolution of Piton des Neiges volcano (La Réunion). Three new hectometer-long outcrops are reported here (Sites 1, 2 and 3) in addition to the gabbroic series (hereafter named Site 4) previously described in the literature. The Sites 1 and 2 are located in the upper parts of the Mât River and show dunite and wehrlite units with no apparent foliation, lineation, or layering. The Sites 3 and 4 are located in the lower parts of the river and are made of olivine-gabbro, gabbro and ferrogabbro units showing marked foliation and lineation, and abundant layering. The mean composition of primary phases varies between Sites 1–2 and Sites 3–4: $Fo_{89.5}$ to $Fo_{69.8}$ in olivine, Mg# of 90 to 69 in clinopyroxene, and Mg# of 44 to 0 in Cr-spinel, titanomagnetite and, ilmenite, respectively. Here we show that the layered gabbros and peridotites exposed at the four sites represent multiple levels of magma storage. Based on the results of previous gravimetric studies and a drill hole related to geothermal exploration, we propose that the gabbroic series belongs to a magmatic system predating the building of Piton des Neiges and centered underneath the cirque of Salazie. The high volume of erupted materials in the NE quadrant of the volcanic edifice, and the southward magmatic flow direction in the layered gabbros suggest that the initial eruptive center of Proto-Piton des Neiges was above the cirque of Salazie, ~3 km north of the present-day summit. The landscape of Piton des Neiges may have changed when its NE flank experienced a major lateral collapse, after complete solidification of the gabbroic bodies. The magmatic activity, then, shifted southward after the flank collapse. Finally, we suggest that peridotites outcrops are associated with the present-day Piton des Neiges.

1 Introduction

Fossil magma chambers are remarkable archives of volcanic systems throughout their lifetime. Magma chambers supplying volcanoes are characterized by partially or entirely molten rock carrying various proportions of crystals, and gradually lose heat and crystallize inwards from their margins (Marsh 2006; Cashman et al. 2017; Jackson et al. 2018; Sparks et

al. 2019; Edmonds et al. 2019). Crustal magma bodies are commonly formed and grown by incremental injections of new magma from depth (Deniel et al. 1987; Annen and Sparks 2002; Glazner et al. 2004; Gudmundsson 2012; Annen et al. 2015; Blundy and Annen 2016; Karakas et al. 2017; Cashman et al. 2017; Sparks et al. 2019). Their internal structures record the compositional evolution, transport dynamics, and mode of crystallization in these systems, while their external structures (size, geometry) are imprints of the storage level, and the volume and frequency of magma transfers (Marsh 2006; Szymanowski et al. 2017; Jackson et al. 2018; Sparks et al. 2019; Edmonds et al. 2019). Having access to such records is critical not only in reconstructing the history of a given volcano, but also in assessing its past behavior and those of other edifices built from the same mantle source.

Probing such systems is, however, a challenge as magma chambers reside deep in the crust and rarely outcrop in active contexts. Similarly to Fuerteventura (Canary Islands; Allibon et al., 2011; Tornare et al., 2016), La Réunion has the advantage of extreme erosion rates (Gayer et al. 2019) providing access to plutonic outcrops related to major volcanic edifices, including one active. Taking La Réunion as one of the archetypes of mafic magmatism and shield volcanism, this contribution focuses on four outcrops of plutonic rocks in the cirque of Salazie; three are newly discovered during our fieldwork along the Mât River. We report here field observations and the mineralogy, petrography and geochemistry for these outcrops in order to constrain the structure of igneous bodies and the magma processes at work in the past activity of Piton des Neiges volcano. These results are placed in the context of the morphological and structural evolution of the volcano, with implications on the magmatic activity of the igneous system.

2 Geological setting

La Réunion is a volcanic island located in the western Indian Ocean, at 700 km east of Madagascar (Fig.1). The island is the current manifestation of the hotspot that produced the Deccan Traps at the K-T boundary, but also intermediately a chain of age-decreasing volcanic constructions consisting of Laccadives, Maldives, Chagos, the Mascarene plateau, and Mauritius (Duncan et al. 1989; Mahoney et al. 2002; Courtillot et al. 2003). Based on radiometric dating of subaerial rocks, current effusive rates and volumetric estimates of the island, La Réunion is thought to be active since at least 5 Ma (Gillot et al. 1994; Lénat et al. 2001) with the edification of two successive shield volcanoes (Fig. 1a): Piton des Neiges, from > 2.2 to 0.029 Ma (McDougall 1971; Quidelleur et al. 2010; Salvany et al. 2012) and

Piton de la Fournaise, from > 0.53 Ma to these days (Gillot et al. 1994). A study of the morpho-structure of the island has shown that the whole edifice is essentially built by the old Piton des Neiges and that the formations of the younger Piton de la Fournaise represent only a small fraction on its eastern flank (Le Friant et al. 2011; Lebas et al. 2018). Piton de la Fournaise volcano is currently in its shield building stage and has been a mainstay for centuries as a natural laboratory for volcanological studies (Vincent 1804; Lacroix 1916; Lacroix 1923; Lacroix 1936). Piton des Neiges is dormant and an important source of information on the past magmatic and volcanic activity of La Réunion hotspot volcanoes. Previous studies have shown that magmas of Piton des Neiges evolved through time with the effusion of basalts and olivine-rich basalts during the shield stage from >2.2 to 0.43 Ma, then consecutive to a period of quiescence of 0.08 Ma, the eruption of plagioclase-rich basalts, hawaiites, mugearites, benmoreites, trachytes and comendites during the postshield stage from 0.35 to 0.029 Ma (Upton and Wadsworth 1966; Upton and Wadsworth 1967; McDougall 1971; Oversby 1972; Nativel 1978; Fisk et al. 1988; Gillot et al. 1994; Kluska 1997; Quidelleur et al. 2010; Smietana 2011; Salvany et al. 2012). The volcanic activity of Piton des Neiges fluctuated considerably during its long life, leading to the building of three successive basaltic shield edifices (before 2 Ma, between 1.4 and 0.95 Ma, and between 0.6 and 0.43 Ma) and two stratocones (between 0.35 and 0.18 Ma, and between 0.14 Ma and 0.029 Ma, McDougall 1971; Gillot and Nativel 1982; Salvany et al. 2012; Gayer et al. 2019).

The morphology of Piton des Neiges is dissected by three major topographic depressions, the cirques of Cilaos, Mafate, and Salazie, from which the internal structure of the volcano is now reachable. The cirque of Salazie has been found to host a plutonic body outcropping in the meanders of the Mât River (Lacroix 1923; Upton and Wadsworth 1972; Chevallier and Vatin-Perignon 1982), described hereafter as Site 4 (Fig. 1b-c). The top of this plutonic body, subjected to many structural studies, is a detachment that led to a northward destabilization of the northern flank of Piton des Neiges (Famin and Michon 2010; Chaput et al. 2014a; Chaput et al. 2014b; Berthod et al. 2016). This northward motion, associated with brittle-ductile deformation and low-temperature hydrothermal alteration (150–250 °C; Famin et al., 2016), occurred during shield building (Berthod 2016).

About 3 km North of Site 4, remnants of a plutonic body have been sampled by the SLZ1 geothermal drill hole (Fig. 1b), from 350 to 1314 m below sea level (bsl; Chovelon, 1986; Demange et al., 1989). These rocks consist of monzogabbros and gabbros (5.97–9.96 wt% MgO in bulk) between 350 and 795 m bsl, and olivine gabbros (30.1 wt% MgO in bulk)

below 795 m bsl. The bottom of the plutonic body is not intersected by the drill hole, but establishes a minimum thickness of 964 m. In parallel with these reports of plutonic rocks in the Mât River and the drill hole, gravimetric and magnetotelluric studies have documented the presence of a large, dense body underneath the volcano, extending from the subsurface down to 4000 m bsl (Malengreau et al. 1999; Gailler 2010; Gailler and Lénat 2012). Finally, another large plutonic body has been identified under the eastern parts of Piton de la Fournaise volcano by gravimetric and magnetotelluric campaigns (Rousset et al. 1989; de Voogd et al. 1999; Malengreau et al. 1999; Gailler et al. 2009; Gailler and Lénat 2010; Gailler 2010; Gailler and Lénat 2012). This plutonic body has been sampled by the SR1 geothermal drill hole (Fig 1a; Lerebour et al., 1989; Rançon et al., 1989; Augé et al., 1989; Rousset et al., 1989) and shown to comprise a succession of gabbros, wehrlites and dunites from top (838 m bsl) to bottom (2831 m bsl). Again, drilling does not reach the bottom of this body but establishes a minimum thickness of 1993m. Although this magma body has been related to submarine lava flows dated at 3.34 and 3.77 Ma (Smietana 2011), the intricacies of its relationships with the past activity of Piton de la Fournaise are still debated (Lénat et al. 2001; Le Friant et al. 2011; Lebas et al. 2018).

3 Field observations

We conducted new field investigations in the inner parts of Piton des Neiges volcano (Fig. 1a-b) and found three new outcrops of plutonic rocks in the cirque of Salazie along the upper course of the Mât River (hereafter labeled Site 1, Site 2 and Site 3, Fig. 1c), each hectometric to pluri-hectometric in size, and located upstream of the gabbroic series of Site 4 described in Upton and Wadsworth (1972). All the plutonic outcrops are crosscut by a network of clinopyroxene- and/or plagioclase-rich veinlets (Fig. 2a). The veinlets are centimetric to decimetric in thickness, and their complexity increases from Sites 1–2 to Sites 3–4. Prehnite-pumpellyite or lower greenschist facies alteration is observed at all sites, but is most apparent at Site 4. Taken together, the four outcrops occur within an area of 2.5 x 1.0 km and all present upper contacts with a pile of sills surmounted by a mafic breccia and crosscut by mafic dykes. These dykes consist of 0.5–1.5-m-thick olivine-rich basalt intrusions dipping 15–30° toward the North. Importantly, the current geometry, i.e. igneous bodies surmounted by sills and a breccia, results from one or several volcano flank destabilizations that likely occurred while the plutonic rocks were already solidified (Famin et al. 2016). The main

features of the four sites are described below.

3.1 Site 1

The plutonic rocks are located in the southernmost part of the area, upstream and at 950–1200 m above sea level (asl), i.e. at a higher elevation than the other plutonic outcrops (Fig. 1c). They are exposed along the river over an area of 600 m north-south and 200 m east-west for a maximum thickness of 250 m. The mass is composed of centimetric- to plurimetric-thick lenses of peridotite separated by mafic intrusions (Fig. 2b). No foliation nor lineation is observed.

3.2 Site 2

The plutonic rocks outcrop about 700 m downstream from Site 1, at 850–940 m asl. Their exposure spreads over 200 m in the direction north-south and 50 m east-west for a thickness of 15–20 m. The plutonic rocks at Site 2 consist of plurimetric-thick layers of peridotite with no apparent foliation or lineation, that gently dip (<10°) toward the north and curve close to the downstream contact with the pile of sills (Fig. 2c). The layers are cut by fractures that produce a network of centimetric to pluri-metric lenses.

3.3 Site 3

The plutonic rocks outcrop about 900 m downstream of those at Site 2. They are exposed over an area of 90 m north-south by 200 m east-west for a thickness of about 20 m at elevations of 750–870 m asl. The eastern and western parts of the plutonic mass are crosscut by a pluri-hectometric syenite intrusion, as detailed in section §3.5. The plutonic rocks of Site 3 consist of a layered gabbro (Fig. 2d-e) with centimetric- to pluri-decimetric-thick layers and a N60 45°S magmatic foliation defined by variations in modal proportion and/or grain-size of olivine, clinopyroxene and plagioclase (Fig. 3). The gabbroic layers show a magmatic lineation with an average orientation N8 48°S (Fig. 3) outlined by pluri-millimetric to centimetric elongated crystals of clinopyroxene and plagioclase. The gabbroic layering is affected by SE-NW trending thrust syn-magmatic faults (Fig. 2d). Layering is ductilely deformed with structures that share similarities to slump structures in sedimentary rocks. These dynamic structures include west-verging overturned folds (Fig. 2e-f), centimetric lenticular schlierens, discontinuous layering, and rare mafic autholiths. The schlierens are generally made of plagioclase crystals and are mostly parallel to the layering.

3.4 Site 4

These plutonic rocks form the outcrop previously described by Upton and Wadsworth (1972). These rocks are exposed about 200 m downstream from those exposed at Site 3, past the syenite intrusion. The plutonic rocks of Site 4 outcrop between 660 and 750 m asl, over a distance of 300 m and, for a thickness of about 20 m. They consist of a fine-layered gabbro with a foliation oriented N92 44°S on average (Figs 2f-g, 3) similar to that observed at Site 3. Their layering tends to be thicker and laminar compared with those of the layered gabbro of Site 3, ranging from centimetric to metric in thickness (Fig. 2g). Similarly to Site 3, the magmatic lineation of the plutonic rocks of Site 4 is defined by the fabrics of elongated crystals of plagioclase and clinopyroxene, although scarcer and more dispersed than there, with an average orientation N212 43°S (Fig. 3). The fine layered gabbro is also affected by several E–W trending reverse faults. Dynamic structures such as slumps and cross beddings are locally observed (Fig. 2f). The northern limit of the gabbroic outcrop corresponds to a detachment fault, gently dipping northward, and in which mafic sills were intruded (Famin and Michon 2010).

3.5 Syenite intrusion

The syenite intrusion crosscuts the layered gabbros of Sites 3 and 4 (Fig. 1c) at 750–850 m asl, over an area of 200 m north-south by 300 m east-west in the Mât River. The second outcrop, located upstream Site 3, is exposed over an area of 200 m north-south by 20 m east-west. The intrusion is fine-grained and massive and thought to be emplaced during the differentiated stage of Piton de Neiges, i.e. with an age younger than 0.35 Ma (McDougall 1971). Unlike the layered gabbros, the syenite does not show any field evidence of prehnite-pumpellyite or lower greenschist facies alteration.

4 Samples & analytical methods

A multi-method approach was carried out to provide an integrated analysis of the four sites. A first set of 44 samples was collected for their petrographic examination (Tab. 1). Among them, 39 samples were used to determine *in situ* chemical compositions of the mineral phases present in the plutonic rocks. The analyses were performed using the CAMECA SX-100 electron microprobe analyzer (EPMA) of the *Laboratoire Magmas et Volcans* (Clermont-Ferrand, France). The beam was set at an accelerating potential of 15 kV and a probe current of 15 nA for major, minor and trace elements (Na, Al, Si, Ca, Fe, Mg, Ti, Mn, K, and P), with 10 s counting times for each element and 20 µm beam diameter. Routine calibration was

performed with a CAMECA set of natural and synthetic mineral standards: orthoclase (K), albite (Na), Al_2O_3 (Al) wollastonite (Si, Ca), fayalite (Fe), forsterite (Mg), $TiMnO_3$ (Ti, Mn), NiO (Ni), Cr_2O_3 (Cr). The same operating conditions were used for olivine, clinopyroxene, plagioclase, and oxides analysis. The second set of 19 samples was used for bulk rock major- and trace-element compositions (4, 2, 8, and 5 samples for Sites 1, 2, 3 and, 4, respectively). The analyses were performed in the Service d'Analyse des Roches et des Minéraux (SARM) at the *Centre de Recherches Pétrographiques et Géochimiques* (Nancy, France). Major elements concentrations were quantified with a Thermo Fischer ICap 6500 ICP-OES on three aliquots of whole-rock powders and completed with trace element analyses by a Thermo Elemental X7 ICP-MS. The samples were prepared for the analyses by fusion with $LiBO_2$ and dissolution with HNO_3. Analytical uncertainty (1σ) is 1 – 15% for major elements and 5 – 15% for minor and trace elements.

5 Results

5.1 Rock types and textures

The representative parageneses and textures of samples are given in Figures 4, 5, and 6, and their modal compositions are given in Table 2. The samples collected at Sites 1 and 2 are peridotitic rocks consisting of dunites and wehrlites containing less than 10 vol% of plagioclase. In contrast, the samples collected at Sites 3 and 4 are principally gabbroic rocks, including olivine gabbros, gabbros, ferrogabbros and anorthosites containing more than 10 vol% of plagioclase. Overall the samples, we noted very little evidence of plastic deformation (such as kink-bands) in the minerals.

5.1.1 Dunites

Dunites are exclusively observed at Sites 1 and 2 where they represent 33% and 44% of the samples, respectively (Fig. 4). They present an adcumulate texture made of olivine (≥ 80 vol%), clinopyroxene (< 5 vol%), and minor oxides (Fig. 5a-b). The olivine crystals are euhedral to subhedral in shape and 0.5–1 cm in diameter and form a cumulus framework. The clinopyroxene crystals are on average smaller than olivines (0.1–1 cm in diameter) and are interstitial in the olivine fabric, with anhedral shapes. Oxide crystals include 10–50 µm Cr-spinel inclusions in the olivine crystals and small ilmenite crystals within the olivine

fractures. Olivine is often partly or entirely altered into serpentine and chlorite.

5.1.2 Wehrlites

The wehrlite samples of Sites 1 and 2 (67 % and 56 % of the samples, respectively; Fig. 4) present a heteradcumulate texture built on interlocking, poikilitic grains of clinopyroxene (15–40 vol%) enclosing crystals of olivine (55–80 vol%), plagioclase (<10 vol%) and oxides (<5 vol%; Fig. 5c-d). The clinopyroxene and olivine crystals are euhedral to subhedral and present a grain size of 0.1–10 mm and 0.2–5 mm, respectively. The oxides consist of euhedral 10–50 µm Cr-spinel inclusions in olivine and anhedral 5–200 µm titano-magnetite crystals enclosed in interstitial position. Three wehrlite samples from Site 2 (CB1230513, CB2230513, and CB4230513 in Table 2) show anhedral to euhedral crystals of plagioclase and sector-zoned clinopyroxene enclosing rounded crystals of olivine (Fig. 5e-f). The wehrlite sample of Site 4 (Fig. 4) presents an adcumulate texture made of 1–3 mm diameter, subhedral to euhedral crystals of olivine and clinopyroxene. The olivine and clinopyroxene crystals are in cumulus and interstitial position, respectively. The plagioclase crystals are interstitial, and 0.3–3 mm in diameter with a subhedral to anhedral shape. The magnetite and ilmenite crystals occur as intergrowths homogeneously distributed in the rock with a grain size of 20–300 µm in diameter. Similarly to the dunites, the olivine crystals in the wehrlites can be partly or entirely altered into serpentine and chlorite, with secondary titano-magnetite in the fractures (Fig. 5e, g). Plagioclase is locally altered into sericite.

5.1.3 Olivine gabbros

Olivine gabbro is a dominant lithology at Site 4 (70% of the samples; Fig. 4). In contrast, it represents 25% of the samples collected in Site 3. The samples are mesocumulates to adcumulates made of cumulus crystals of olivine (2–45 vol%) and clinopyroxene (39–55 vol%) embedded in interstitial plagioclase (15–49 vol%) and oxides (Fig. 6a-b). The crystals of olivine and clinopyroxene are subhedral to euhedral and > 1 mm in diameter, except for one sample (SAL111) in which the olivine crystals are euhedral and in interstitial position. Plagioclase occurs in the olivine gabbro samples as large crystals (0.4 to 1 mm) with anhedral to euhedral shapes and both cumulus and interstitial positions. The oxide crystals consist of intergranular titano-magnetite intergrowth with ilmenite, homogeneously distributed in the rock. Minor phlogopite (< 1 vol%) occur as small anhedral crystals (< 100 µm) in association with clinopyroxene and plagioclase. Olivine displays various degrees of iddingsitization, most

apparent at Site 4. Clinopyroxene can be partly or entirely replaced by uralitic amphibole and chlorite. Plagioclase may be altered into sericite and albite. Successive mineralization of prehnite, zeolite, and calcite are observed in fissures.

5.1.4 Gabbros

The gabbro rock type represents 25 and 15% of the samples collected at Sites 3 and 4, respectively (Fig. 4). The samples display an adcumulate to mesocumulate texture characterized by fine-grained crystals of clinopyroxene (44–80 vol%; Fig. 6c-d) and plagioclase (20–54 vol%). The clinopyroxene crystals are in cumulus position and have a stubby shape and a grain size in the range 0.05–0.3 mm. Plagioclase crystals are subhedral to euhedral tablets in cumulus or interstitial position with a grain size ranging from 0.2 to 1 mm, defining a strong fabric. The samples contain also minor oxides (1–5 vol%) consisting in intergrown crystals of titano-magnetite and ilmenite. As for olivine gabbros, magmatic minerals locally show evidence of uralitic and/or sericitic alteration.

5.1.5 Ferrogabbros

The ferrogabbros of Site 3 (42% of the samples) and Site 4 (10%) have a texture similar to the above-mentioned gabbro samples, except that they contain up to 5 vol% of Fe-Ti oxides crystals in cumulus and interstitial position and a lower abundance of clinopyroxene and plagioclase in cumulus and interstitial position (25–50 vol% and 40–45 vol%, respectively; Fig. 6e–f). Several samples display a slightly greater range of grain sizes but are not distinctly porphyritic in appearance. The clinopyroxene crystals present also a stubby shape with a grain size in the range 0.05–0.3 mm. Plagioclase shows a tabular shape and a grain size of 0.2–1 mm that define, in some cases, a strong fabric (Fig. 6e–f). Local alteration is similar to that of other gabbros.

5.1.6 Anorthosites

The anorthosites occur only as veinlets that crosscut the plutonic masses at Sites 1, 2, 3, and 4. The samples collected at Site 3 are made of cumulus crystals of plagioclase (~ 96 vol%), clinopyroxene (~ 3 vol%), and sparse Fe-Ti oxide (< 1 vol%) forming an adcumulate texture. The plagioclase and clinopyroxene crystals show euhedral to subhedral shapes with a grain size ranging from 0.1 to 1.5 mm. Anorthosites are locally altered into assemblages of chlorite + sericite + albite + zeolite ± calcite.

5.1.7 Syenite

The syenite intrusion crosscutting Sites 3 and 4 is composed of sub-euhedral alkali feldspar (< 10 vol%, <500 μm) and amphibole (<1 vol%, up to 5 mm) macrocrysts, embedded in a groundmass containing microcrysts of elongated plagioclases, sodic pyroxenes, and Fe-Ti oxides. Unlike the layered gabbros, the syenite can be vesicular. Vesicles are filled with calcite.

5.2 Chemical composition of minerals

Representative chemical compositions of olivine, clinopyroxene, plagioclase, and oxides are given in Tables 3–6 and plotted in Figures 7–10. Compositional zoning is weak or absent in the samples, hence only representative compositions were reported for each mineral.

5.2.1 Olivine

The data given in Table 3 and Figure 7 indicate that two olivine groups can be distinguished based on their Fo content: Fo-rich olivine at $Fo_{>81}$ in the peridotites of Site 1 ($Fo_{84.1–87.9}$) and Site 2 ($Fo_{81–89.5}$), and Fe-rich olivine at $Fo_{<80}$ in the gabbros of Site 3 ($Fo_{75.2–76.4}$) and Site 4 ($Fo_{69.8}$–$Fo_{79.3}$). Among the Fo-rich group, the olivine grains in the dunites present a scattered Fo distribution with a mode at $Fo_{82.5}$ (in samples from Site 2) and two other main populations at $Fo_{87.5–88}$ (Sites 1 and 2) and $Fo_{89.0–89.5}$ (Site 2 only; Fig. 7). The wehrlites show similar olivine compositions to the dunites but with the main mode around $Fo_{85.5}$ (Fig. 7). The olivine composition at $Fo_{89.5}$ in dunite from Site 2 represents one of the highest Fo content measured in the subaerial domain of La Réunion, after the highest value at $Fo_{90.6}$ reported by Sobolev and Nikogosian for olivine of Piton des Neiges (1994). Among the Fe-rich olivine group, three populations can be observed in the olivine gabbros of Sites 3 and 4: the main mode at $Fo_{73–77}$ and two less represented populations at $Fo_{70–70.5}$ and $Fo_{78.5–79}$ (Fig. 7). It is important to note that interstitial olivine has a composition similar to cumulus olivine.

The CaO contents of olivine, plotted in Figure 7b, may be classified into three populations: (1) a low CaO (0.05–0.20 wt%), high $Fo_{84–89}$ population in dunites and wehrlites from Sites 1 and 2; (2) a high CaO (0.20–0.40 wt%), high Fo_{80-89} population only found in the dunites and wehrlites of Site 2; (3) A low CaO (~0.01–0.12 wt%), low $Fo_{70–79}$ population in the wehrlite and olivine gabbros of Sites 3 and 4. Importantly, the olivine grains of the population (2) show rounded contours in the wehrlites (Fig. 5e-h) and their compositions are similar to that of olivine-bearing lavas erupted at Piton de la Fournaise (Boudoire et al. 2019).

351

352 5.2.2 Clinopyroxene

353 Clinopyroxene compositions are presented in Figure 8. A correlation is observed between
354 the Mg# of clinopyroxenes and the rock, as the most mafic rocks (Sites 1 and 2) contain high-
355 Mg# clinopyroxenes whereas evolved rocks (Sites 3, 4) contain lower Mg# clinopyroxenes
356 (Fig. 8a). The clinopyroxene crystals of Site 1 consist of ~En_{48} $Fs_{7}Wo_{45}$ diopside at Mg# =
357 86–89, with 0.03–1.18 wt% Cr_2O_3 and 3.37–3.70 wt% Al_2O_3 (Tab. 4, Fig. 8a, b, and c). The
358 clinopyroxene crystals of Site 2 have more variable compositions at $En_{38–49}Fs_{5–17}Wo_{39–48}$ and
359 Mg# = 69–90 spread over the fields of diopside and augite, with Cr_2O_3 contents ranging from
360 below the detection limit to 1.41 wt% and Al_2O_3 contents at 1.07–5.99 wt%. These variations
361 might correspond to sector zoning observed in some samples (Fig. 5g-h). Clinopyroxene
362 crystals at Site 3 are also diopside/augite at $En_{40–46}Fs_{8–16}Wo_{40–47}$, with a Mg# at 73–84, Cr_2O_3
363 ranging from below the detection limit to 0.69 wt% and Al_2O_3 from 0.99 to 5.18 wt%. The
364 clinopyroxene crystals of Site 4 are diopside/augite at $En_{40–46}$ $Fs_{7–15}Wo_{42–49}$ with Mg# in the
365 range 73–86, less than 0.55 wt% Cr_2O_3, and 0.88 to 8.07 wt% Al_2O_3. It is important to note
366 that the Cr_2O_3 content of clinopyroxene decreases with the Mg# from the peridotites of Sites 1
367 and 2 to the gabbroic rocks of Sites 3 and 4 (Fig. 8b).

368

369 5.2.3 Plagioclase

370 As a general observation, the composition of plagioclase is bimodal in the layered gabbros
371 and peridotites, with a high anorthite population (An_{65-81}) observed at Sites 1, 3, 4, and a
372 lower anorthite population (≤ An_{65}) found at Sites 2, 3, 4 (Fig. 9a). The plagioclase crystals
373 occurring in the anorthosite veinlets of Site 1 have a composition at $An_{77–82}Ab_{18–22}Or_{0.4–0.9}$
374 (Tab. 5). The plagioclase crystals of the wehrlites of Site 2 show chemical compositions that
375 are either intermediate (~ An_{57}) or albitic (~ An_{06}), a probable result of late alteration. The
376 plagioclase crystals of Site 3 are $An_{51–82}$ grains with some albitic individuals at $An_{14–23}$
377 (gabbro sample CB7230513). The plagioclase crystals of Site 4 occur mainly as $An_{47–87}$
378 grains. Plotted in K_2O vs. An space (Fig. 9b), the K_2O content of plagioclase increases overall
379 from 0.07–0.16 wt% at Site 1, to 0.12–0.35 wt% to Site 2, and to 0.03–0.64 wt% at Sites 3
380 and 4. We note that the composition range at $An_{75.3–82.2}$ of plagioclase in the anorthositic
381 veinlets of the Site 3 is similar to that of the plagioclase crystals observed in the anorthositic
382 veinlets of the Site 1.

383

384 5.2.4 Oxides

385 The oxides include Cr-spinel, titanomagnetite and ilmenite. We note that Cr-spinel and
386 titanomagnetite crystals do not contain internal Ti-rich exsolutions. Their compositions are
387 given in Table 6 and illustrated Figure 10. Cr-spinel crystals in the dunites and the wehrlites
388 of Sites 1 and 2 show overlapping compositions with high contents in Cr_2O_3 (26.32–45.24
389 wt%) and FeO_t (24.64–41.70 wt%), and moderate amounts of Al_2O_3 (8.77–17.77 wt%), MgO
390 (4.95–10.60 wt%) and TiO_2 (1.05–6.27 wt%). No Cr-spinel was observed at Sites 3 and 4,
391 and no titanomagnetite was observed at Sites 1 and 2. The titanomagnetite crystals at the Sites
392 3 and 4 show overlapping compositions, with contents at 2.89–26.35 wt% TiO_2, 1.49–9.81
393 wt% Al_2O_3, and 47.97–82.10 wt% FeO_t. Only two magnetite crystals were found in the study
394 area and only at Site 4: one at 88.65 wt% FeO_t in a wehrlite, and another at 80.17 wt% FeO_t
395 in an olivine gabbro. Their composition is distinct from the titanomagnetite crystals with
396 contents in TiO_2 and Al_2O_3 lower than 1 wt% (Fig. 10a). The ilmenite crystals were found in
397 all types of plutonic rocks of Sites 2, 3, and 4 except in the wehrlites. Their chemical
398 compositions are in the range 43.2–54.89 wt% TiO_2, 0.03–1.28 w% Al_2O_3, and 38.35–52.35
399 wt% FeO_t. It is important to note that their FeO_t content increases while their TiO_2 content
400 decreases from the dunites of Site 2 to the olivine gabbros, gabbros and ferrogabbros of Sites
401 3 and 4 (Fig. 10).

402

403 ## 5.3 Whole-rock geochemistry

404 The whole-rock composition of samples is reported in Table 7 and plotted in Figure 11.
405 Consistent with our petrographic analysis, the plutonic rocks of Sites 1 and 2 show ultramafic
406 compositions with high MgO contents (32.96–42.58 wt%) and low SiO_2, CaO, and TiO_2
407 contents (36.11–39.92 wt%, 0.72–4.23 wt%, and 0.16–0.74 wt%, respectively; Fig. 11). This
408 contrasts with the differentiated compositions of plutonic rocks at Sites 3 and 4 with more
409 intermediate MgO, SiO_2, CaO, and TiO_2 contents (6.75–22.06, 39.98–48.31, 11.36–16.66
410 wt%, and 0.70–4.93 wt%, respectively). Related to their various modes and mineralogy, the
411 olivine gabbros, gabbros and ferrogabbros show distinct chemical compositions, which are
412 best observed in the SiO_2 vs. TiO_2 space (Fig. 11d). The olivine gabbros have intermediate
413 contents in SiO_2 and low contents in TiO_2 (43.52–46.04 wt% and 0.70–0.93 wt%,
414 respectively), the gabbros have high contents in SiO_2 and intermediate contents in TiO_2

(46.30–48.31 wt% and 0.74–1.51 wt%, respectively), and the ferrogabbros are defined by low contents in SiO_2 and high contents in TiO_2 (39.98–41.88 wt% and 3.14–4.93 wt%, respectively). The sample CB2260513 has been classified as a gabbro under the microscope, but since it has 18.18 wt% FeO in bulk composition, it should be classified as a ferrogabbro instead. The chemical composition of rocks samples collected at Site 3 tends to overlap with five of the samples from the SLZ1 drill hole and referenced K31 through K35 (gabbros at 46.5–50 wt% SiO_2; 6.08–9.96 wt% MgO; 10.81–12.65 wt% CaO; 2.01–2.75 wt% TiO_2; Chovelon, 1986; Demange et al., 1989). One sample of olivine gabbro (K42) from the drill hole shows an intermediate mafic composition at high MgO (27.7 wt%) and low SiO_2, CaO and TiO_2 contents (43.9 wt%, 7.29 wt%, and 0.35 wt%, respectively) between the Sites 1–2 and the Sites 3–4.

The trace element composition of samples is given in Figure 11e. The chondrite-normalized REE enrichment patterns of dunites and wehrlites from Sites 1 and 2 appear similar and follow a simple slope of depletion as the atomic number increases from La to Lu (i.e. from LREE to HREE), with no Eu anomaly except for one sample from Site 2 (CB1150914). It is important to note that this pattern is similar and remarkably parallel to that of the erupted products of Piton des Neiges during its basaltic and differentiated stages, despite the 2 to 30 times dilution of REE in peridotites. The enrichment patterns of olivine gabbros, gabbros, and ferrogabbros of Sites 3 and 4 are similar to that of the dunites and wehrlites of Sites 1 and 2, at the difference that they have a marked depletion in LREE and a clear positive Eu anomaly. These rocks show relatively high concentrations in Gd to Lu in comparison with the erupted products of Piton des Neiges, with dilution factors of only 1 to 4. The samples show also two trends in the Th vs. Sm space (Fig. 11f): variable enrichments in Th and low Sm contents for the peridotitic rokcs at Sites 1–2, and low Th and high Sm contents for the gabbroic rocks at Sites 3–4.

6 Discussion

6.1 Peridotites and layered gabbros

Previous studies on the gabbroic mass outcropping at Site 4 have suggested that these rocks are remnants of an ancient magma body that supplied the volcanic activity of Piton des

Neiges (Upton and Wadsworth 1972; Chevallier and Vatin-Perignon 1982; Upton et al. 2000; Pronost 2001). The structural and textural characteristics of these rocks, have indicated a variety of magmatic processes, including fractional crystallization, crystal settling, convection, and slumps. Our investigations in the Mât River reported three new plutonic outcrops (Sites 1, 2, and 3, Fig. 1c), which, combined with Site 4, offers a unique opportunity to scrutinize *in situ* the frozen dynamics of magma flowing and cooling within the magmatic system of Piton des Neiges volcano.

6.1.1 Peridotitic units

Sites 1 and 2 host peridotitic lithologies (dunites and wehrlites, Figs 4 and 5) and are primitive in nature, having abundant Mg- and Cr-rich minerals ($Fo_{81–89.5}$ olivine, clinopyroxene at Mg# = 69 – 90, and Cr-spinel at 26.32 – 45.24 wt% Cr_2O_3, (Figs 7, 8, 10 and 12), and high bulk MgO contents (32.96–42.58 wt%, Fig. 11). A first assumption is that all those rocks are imprints of the crystallization of high-temperature and high-MgO magmas. The primitive composition of the peridotites and the lack of any evidence of tectonic exhumation suggest that these magmas did not significantly differentiate in deep storage before their crystallization at shallow levels (≤ 2.5 km depth) in the volcanic edifice.

According to the olivine-augite Mg-Fe-exchange geothermometer of Loucks (1996), the re-equilibration of the peridotite layers would have happened in the range 1130–1165 ± 6 °C (Tab. 8). The peridotites display adcumulate and heteradcumulate textures in which clinopyroxene was clearly the second silicate phase to precipitate after olivine (Fig. 5). REE patterns confirm our textural observations and reject the cumulative origin of the clinopyroxene (Fig. 11e-f). The adcumulate peridotites may be interpreted as the result of melt segregation, settling, and accumulation (Coats 1936; Tait and Jaupart 1996; Cawthorn 1996) or *in situ* crystallization on the magma reservoir margins (Campbell 1977; Walker et al. 1988; Marsh 1996).

The fact that the peridotites at Sites 1 and 2 have a similar enrichment pattern in REE with the erupted products of Piton des Neiges volcano (Fig. 11f-e) suggests that the two are related genetically. These outcrops represent the first tangible evidence of a primitive, consolidated magma body at Piton des Neiges volcano, which was inferred indirectly from gravimetric surveys (Malengreau et al. 1999; Gailler and Lénat 2012) and the presence of peridotitic xenoliths in the erupted products (Upton and Wadsworth 1972; Upton et al. 2000).

Finally, the fact that the peridotites are crosscut by thick anorthositic veinlets indicates a late transport of residual melts through the plutonic rocks after partial to complete solidification (Pallister and Hopson 1981). Given the geochemical similarity of the host rocks and veinlets, it is likely that these anorthositic melts result from local mineral and melt segregation (Figs 9 and 12).

6.1.2 Layered gabbros

The plutonic rocks outcropping at Sites 3 and 4 present more differentiated compositions, with gabbroic lithologies (wehrlites, olivine gabbros, gabbros, ferrogabbros and anorthosites, Figs 4 and 6), intermediate mineral compositions ($Fo_{69–79}$ olivine, clinopyroxene at Mg# = 73 – 86, $An_{47–87}$ plagioclase, and FeTi-oxides, Figs 7–10 and 12), and moderate to low bulk MgO contents (6.75–22.06 wt%, Fig. 11). These outcrops provide evidence of crystallization from magmas having an intermediate composition. The estimated temperatures of re-equilibration from Loucks (1996) suggest that the gabbroic layers of Sites 3 and 4 were at about 1039 – 1118 ± 6 °C, i.e. at temperatures lower than the peridotites at Sites 1 and 2 (Tab. 8). The thin layering, the pronounced lineation, and the abundance of discontinuous and folded layering, syn magmatic faults, cross bedding and schlierens at Site 3 (Fig. 2d-f) suggest a high-energy environment (Wager and Brown 1967; McBirney and Noyes 1979; Hunter and Sparks 1987; Hoover 1989; McBirney and Nicolas 1997; Irvine et al. 1998; McBirney 2009). In contrast, the magmatic flow at Site 4 appears relatively more regular and laminar, with scarcer structures relatable to a high-energy environment (Fig. 2g-f). Any single or even a few cases of igneous layers can be successfully explained by one or a combination of several mechanisms (Cawthorn 1996). It is important to note that Berthod (2016) showed that the plutonic body occurring in the Mât River displays the same palaeomagnetic signature than La Montagne massif (Quidelleur et al. 2010) and consequently suggests that the plutonic rocks outcropping at Site 3 were not tectonically tilted from their since 2.2 Ma. Thus, because layering have not been moved from their original position and are strongly inclined (43–44°S, Fig. 3), we suggest that the dynamic structures observed at Sites 3 and 4 were sorted and deposited by settling and magmatic crystal-liquid suspension currents, sometimes coupled with convective boundary-layer currents (Irvine et al. 1998). It is also likely that convective turbulences occurred in the reservoir through the influxes of fresh mafic magma into the chamber (Jaques 1981; Holness 2005).

We consider two different origins for these magmas: either they come from deeper levels in the edifice (following the classic model of shield building after Wolfe et al., 1997), or they come from the differentiation of primitive magmas at a similar level in the edifice. The fact that the gabbroic rocks at the Sites 3–4 show different enrichment patterns, with a relative depletion in LREE, may indicate either a different magma, a mixing between the magma at Site 1–2 and another one, or fractionation processes within the same source. In the latter case, the change in enrichment pattern can be explained by extensive fractionation and accumulation of clinopyroxene (which are abundant in the peridotitic lenses but even more in the gabbroic layers; Table 2) given that this mineral has a higher affinity for HREE than for LREE (Duncan et al. 1989; Blundy and Wood 1994; Johnson 1998; Norman et al. 2005; Peters et al. 2016; Barrat and Bachèlery 2019). We note that clinopyroxene accumulation is evidenced by whole-rock and mineral geochemistry (Figs 11b-d and 12c).

Similarly to the veinlets in the peridotite units, we interpret the anorthositic veinlets in the layered gabbros as residues of late liquids that crosscut the plutonic bodies after their partial to complete solidification (Pallister and Hopson 1981).

6.2 Pluton dynamics: single reservoir or stacked intrusions?

Gravimetric and magnetotelluric studies, as well as the SLZ1 borehole, indicate a large (pluri-kilometric in diameter) igneous body underlying the cirque of Salazie. The four outcrops described here are inferred to belong to this large plutonic complex. Nevertheless, our field investigations also show that the four distinct plutonic outcrops are separated from each other by sheet intrusions and breccia deposits (Fig. 1c), it is unclear whether these outcrops correspond to four different magma bodies or to subparts of larger structures.

Given their similar textures (Fig. 5) and mineral chemistry (Figs 7–12 and Tab. 9) and the proximity of the outcrops (Site 1 at 950–1200 m asl, Site 2 at 850–940 m asl, and only ~700 m apart, Fig. 1c), it is likely that the peridotitic units at Sites 1–2 belong to the same plutonic complex. Similarly, the gabbroic rocks at Sites 3–4 have close textures (Fig. 6), mineral chemistry (Figs 7–12 and Tab. 9), and dynamic structures (Fig. 2) and they are located in the same vicinity (Site 3 at 750–870 m asl, Site 4 at 660–750 m asl, and only ~200 m apart, Fig. 1c), which, taken together, suggest that these gabbroic rocks might be parts of a same plutonic complex.

543 The question then arises as whether these gabbroic and peridotitic units correspond to a
544 single petrologically and geochemically zoned magma reservoir (e.g., Skaergaard; Wager and
545 Deer 1939; Wager and Brown 1968; McBirney 1995; Tegner et al. 2009a; Salmonsen and
546 Tegner 2013), or to a stack of several independent intrusions as for many other layered
547 plutons (Glazner et al. 2004; Morgan et al. 2008; Michel et al. 2008; Grocott et al. 2009;
548 Leuthold et al. 2012; Leuthold et al. 2014). In an attempt to answer that question, the essential
549 features of each site are summarized and compared in Table 9.
550
551 The single reservoir hypothesis is supported by trends in the whole-rock geochemistry,
552 showing a northward decrease in MgO and an increase in SiO_2, CaO, Na_2O, K_2O and Fe_2O_3
553 in the order Site 1 => Site 2 => Site 4 => Site 3 (Tabs 7 and 9, Fig. 11). Accordingly, the
554 forsterite content in olivine, the Mg number in clinopyroxene and the oxides, and the
555 anorthite content in plagioclase all tend to decrease from one site to another according to the
556 same sequence (Figs 7–10). This would hence point to fractional crystallization as the main
557 magmatic process in a unique magma reservoir, yielding to the compositional evolution of the
558 magma from mafic at Sites 1–2, to intermediate at Sites 4–3 (Fig. 12). However, this
559 sequence of differentiation may appear incomplete since there are notable gaps in whole-rock
560 and phase compositions between the Sites 1–2 and the Sites 4–3 (Figs 7–12 and Tab. 9). One
561 possibility for these gaps is the lack of exposed series in between these sites. The peridotitic
562 series and the gabbroic series only outcrop 900 m apart in the Mât River (Fig. 1c), and it is
563 hence possible that, in between, buried under the breccia, lies a third mass of plutonic rocks
564 that connects the Sites 1–2 to the Sites 4–3. In this case, the buried series would contain the
565 rest of the plutonic record, with layers transitioning in chemical composition and mineral
566 assemblage from peridotitic to gabbroic lithologies.
567 However, the single reservoir interpretation is complicated by the fact that the peridotitic
568 units of Sites 1–2 occur at higher altitudes than the gabbroic ones of Sites 4–3, since the most
569 mafic layers are usually set at the base of magma chambers and more differentiated layers
570 atop (Cawthorn and Walraven 1998; Cawthorn 2007; Tegner et al. 2009b; Salmonsen and
571 Tegner 2013). This forces us to consider that the succession of Sites 1–2–4-3 is an inverse
572 plutonic sequence, which would thus correspond to a roof of the magma chamber. Layered
573 series are not always observed in the upper parts of mafic reservoirs, perhaps because they
574 seldom form in these regions, or because their preservation is more subject to magma
575 dynamics and weathering than the lower series (Jaupart and Tait 1995). However, the
576 processes related to their formation have been described in the upper parts of several sills,

intrusions, and lava lakes (e. g. Simkin 1967; Brown and Wager 1968; Helz et al. 1989; Latypov et al. 2007). One obstacle to that hypothesis is the compact texture of peridotitic layers at Sites 1–2, which seem particularly difficult to achieve in a context of density inversion where the crystals lay atop the melt. But many crystals would be locally plated by laminar currents against the margins of the magma chamber (McBirney and Noyes 1979; Pallister and Hopson 1981; Irvine 1982; Nicolas et al. 2009), and even grow behind the solidification front, trapped within the viscous melt (Marsh 1996; Marsh 2006). In fact, these processes could be consistent with the presence of residual glass in between the crystals of some of the samples (Fig. 5g-h). Given that the melt concentrates incompatible elements such as Sm and Th, the presence of interstitial glass in the peridotites of Sites 1–2 could explain their high Sm and Th contents. In contrast, the glass-poor gabbros of Sites 4–3 shows variable and low Sm contents. Moreover, the adcumulate textures observed in several samples from Sites 1–2 could be also consistent with crystallization and maturation of olivine within a thermal gradient (Walker et al. 1988).

Given the difficulties in interpreting the Site 1–2–4-3 sequence as belonging to a single zoned magma reservoir, it seems more plausible to consider that the sequence observed at Sites 1–2–4-3 represents a stack of several independent intrusions. Contrasted chondrite-normalized REE enrichment patterns (Fig. 11e) and Sm/Th behaviors (Fig. 11f) between Sites 1–2 and Sites 4–3 support this second interpretation. Moreover, because the REE enrichment of a parental magma undergoing extensive fractionation of clinopyroxene should be lower than that of the daughter liquid, the layered gabbroic rocks cannot derive from peridotitic magmas. Furthermore, the layered gabbros and the peridotites outcrops are separated by magmatic intrusions and breccia deposits, which is consistent with these outcrops representing distinct magma bodies (Figs 1c and 13a). All these lines of evidence seem to indicate that the plutonic rocks outcropping at Sites 1, 2, 3, and 4 by the Mât River represent at least two different intrusions, one peridotitic (Sites 1–2) and another one gabbroic (Sites 4–3). In this respect, the plutonic rocks excavated at SLZ1 drillhole might belong to the second intrusion. In consequence, we suggest that the plutonic complex of Piton des Neiges is more likely made by incremental stacking of several independent magma intrusions, rather than by solidification of a single large magma reservoir. Separated magma intrusions are consistent with the inferred plumbing system of shield volcanoes in which magmas are stored in distinct, small ponding zones and/or sills (Lénat and Bachèlery 1990; Poland et al. 2009; Peltier et al. 2010; Montgomery-Brown et al. 2011; Baker and Amelung 2012; Di Muro et al. 2014) and

support the assumption that the feeding system of a volcano can be made of an array of sills and dykes grown incrementally by an amalgamation of new magmatic injections (Deniel et al. 1987; Annen and Sparks 2002; Glazner et al. 2004; Gudmundsson 2012; Annen et al. 2015; Blundy and Annen 2016; Karakas et al. 2017; Cashman et al. 2017; Sparks et al. 2019).

6.3 Stages of pluton growth in the evolution of Piton des Neiges

The original volcanic summit was ~3.5 km asl (Fig. 13b) and these plutonic rocks outcrop at 650 to 1000 m asl. This implies that the magma was stored at ~2.5 km below the surface. This depth is consistent with the physical model of Ryan (1987) in which magmas are preferentially stored at levels of neutral buoyancy, commonly corresponding to depths of 2 – 4 km below volcanic edifices (Ryan 1988; Fodor and Galar 1997; Albarède et al. 1997; Bureau et al. 1998; Battaglia et al. 2005; Scoates et al. 2008; Welsch et al. 2009; Peltier et al. 2009; Famin et al. 2009; Allibon et al. 2011; Lénat et al. 2012; Baker and Amelung 2012; Larrea et al. 2013). The Piton des Neiges volcano is situated ~7 km above the ocean floor, which inhibits direct transfer of magma from deep crustal levels to the summit zone (Pinel and Jaupart 2000) and favours shallow crustal storage.

However, the striking differences between Sites 1–2, and Sites 4–3, in terms of petrology, geochemistry and structure, raise the question of their relationship and their integration in the evolution of Piton des Neiges volcano.

Indeed, the gabbroic series of Sites 4–3 are clearly discordant with the formations of Piton des Neiges due to the development of a main detachment that cuts the plutonic body during the shield building stage of Piton des Neiges while the gabbroic rocks were at a temperature < 250°C (Famin and Michon, 2010; Famin et al., 2016). The gabbroic series also show a marked depletion in LREE that makes a genetic link between these plutonic rocks and the mafic and differentiated lavas of Piton des Neiges rather unlikely. Conversely, the clinopyroxene crystals of the layered gabbros have geochemical affinities with those found as phenocrysts in the ankaramites of the La Montagne massif (2.1 – 1.9 Ma), on the northern flank of Piton des Neiges (McDougall and Watkins 1973; Quidelleur et al. 2010). In addition, the series at Sites 4–3 have petrological and geochemical similarities with the plutonic rocks excavated by the SLZ1 drill hole in the cirque of Salazie (Fig. 1b). These comparisons suggest that the gabbroic plutonic intrusion extends north of the observed outcrops. The southward dip of the gabbro layers at Sites 4–3 corroborates this interpretation by suggesting

643 that the gabbro unit is bulged northward. Based on their study of depocenters, Lebas et al.
644 (2018) concluded that the eruptive center of Piton des Neiges in its first construction phase
645 ("Proto-Piton des Neiges") was located several kilometers north of the more recent eruptive
646 center corresponding to the actual summit. It is thus tempting to attribute the gabbroic part of
647 the plutonic complex of Piton des Neiges to the La Montagne phase (Quidelleur et al. 2010;
648 Salvany et al. 2012), associated with an eruptive center located in the cirque of Salazie (Fig.
649 13b, EC Proto-PdN).

650 The presence of a detachment zone overlain by a breccia unit made of basaltic lavas at the
651 contact with the plutonic rocks of Site 4 suggests that the plutonic complex was at the root of
652 a large flank destabilization (Famin and Michon 2010; Chaput et al. 2014a; Berthod et al.
653 2016). The discordant contact between the layered gabbro and the debris avalanche deposits
654 shows that the flank collapse removed a large part of the plutonic complex (Berthod 2016;
655 Berthod et al. 2016). The collapse occurred once the upper parts of the layered gabbros were
656 already solidified (Famin et al. 2016). We thus propose that the lateral offset between the
657 summit of Piton des Neiges to the south (Fig. 1) and the deep dense body underlying the
658 cirque of Salazie results from this structural failure that led to a migration of the volcanic
659 center to the south (EC PdN in Fig. 13b, Gailler and Lénat 2012). The presence of a deeper
660 dense body underlying the cirque of Cilaos revealed by geophysical data (Gailler and Lénat
661 2012) supports this assumption.
662
663 The mineral and whole-rock compositions of the peridotites of Sites 1–2, positioned at the
664 foot of the current summit of Piton des Neiges (Figs 1 and 13b), are consistent with both the
665 crystallization of Mg-rich magmas and the eruption of basalts and olivine-rich basalts during
666 the shield-building stage of Piton des Neiges (Fig. 11). Moreover, the sills of peridotites at the
667 Site 2 show a northward gentle dip concordant with those of the sills related to the basaltic
668 period of Piton des Neiges (Fig. 2c). Therefore, we tentatively interpret the peridotites of Sites
669 1–2 as part of the magmatic system of Piton des Neiges (Fig. 13b, EC PdN). The primitive
670 mineral compositions of the peridotites of Sites 1–2 suggest that these rocks crystallized from
671 poorly differentiated magmas similar to those observed along the NW rift zone between Piton
672 des Neiges and Piton de la Fournaise (Boudoire et al. 2019).

673 Finally, a batch of more differentiated magma was then intruded after the cooling of the
674 peridotites and layered gabbros, yielding the syenite plutonic mass (younger than 0.35 Ma

according to McDougall, 1971) inserted in between the Sites 3 and 4 during the Phase IV of the Piton des Neiges (Page 1994).

7 Conclusions

Our petrological study of the plutonic rocks outcropping at Sites 1, 2, 3, and 4 of the Mât River provides new insights on the magmatic system of Piton des Neiges volcano. The four outcrops consist of dunites and wehrlites overlying layered olivine gabbros, gabbros, and ferrogabbros. The dunite and wehrlite layers may correspond to the lower parts of a magma reservoir, formed by crystal separation from a primitive magma, settling and accumulation as evidenced by their adcumulate and heteradcumulate textures. In contrast, the olivine gabbro, gabbro and ferrogabbro layers define a zone formed from differentiated magmas in a high-energy environment, as evidenced by the presence of overturned folds, schlierens, and discontinuous layering. These plutonic outcrops have diverse structural, textural and compositional features, and are interpreted as remnants of at least two independent magma bodies: one peridotitic and the other gabbroic. These two systems were active at different periods of time. The differences in whole rock and phase compositions of layered gabbros and peridotites support this hypothesis. Hence, we propose that the four outcrops are parts of a pluri-kilometric composite plutonic complex, built by successive stacks of genetically unrelated magma intrusions over the entire lifetime of shield-building. Pluton growth began with gabbroic magmas emplaced from a volcano center located in the cirque of Salazie, and then shifted to more mafic magma compositions, emplaced from a southward volcano center corresponding roughly to the present-day Piton des Neiges summit.

ACKNOWLEDGMENTS

We thank Pierre Belle for his participation in the fieldwork and Genevieve Lebeau for preparing the thin sections. This work is a part of a Ph.D. fellowship sponsored by Fonds Social Européen and Région Réunion. We thank James Scoates, an anonymous reviewer, and Editor Kelly Russell for constructive criticism and help in improving the manuscript. Chemical analyses were funded by INSU-CNRS grants “Sill’nSlip” and “Runrise”. This is IPGP contribution 4163. This is Laboratory of Excellence ClerVolc contribution number 431.

REFERENCES

706 Albarède, F., Luais, B., Fitton, G., Semet, M., Kaminski, E., Upton, B.G.J., Bachélery, P.,
707 Cheminée, J.-L., 1997. The geochemical regimes of Piton de la Fournaise Volcano
708 (Réunion) during the last 530 000 years. J. Petrol. **38**, 171–201.
709 https://doi.org/10.1093/petroj/38.2.171
710 Allibon, J., Bussy, F., Lewin, É., Darbellay, B., 2011. The tectonically controlled
711 emplacement of a vertically sheeted gabbro-pyroxenite intrusion : Feeder-zone of
712 an ocean-island volcano (Fuerteventura , Canary Islands). Tectonophysics **500**,
713 78–97. https://doi.org/10.1016/j.tecto.2010.01.011
714 Annen, C., Blundy, J.D., Leuthold, J., Sparks, R.S.J., 2015. Construction and evolution of
715 igneous bodies: Towards an integrated perspective of crustal magmatism. Lithos
716 230, 206–221.
717 Annen, C., Sparks, R.S.J., 2002. Effects of repetitive emplacement of basaltic intrusions on
718 thermal evolution and melt generation in the crust. Earth Planet. Sci. Lett. **203**,
719 937–955.
720 Augé, T., Lerebour, P., Rançon, J.-P., 1989. The Grand Brûlé exploration drilling: New data
721 on the deep framework of the Piton de la Fournaise volcano. Part 3: Mineral
722 chemistry of the cumulate rocks. J. Volcanol. Geotherm. Res. **36**, 139–151.
723 https://doi.org/10.1016/0377-0273(89)90010-3
724 Baker, S., Amelung, F., 2012. Top-down inflation and deflation at the summit of Kilauea
725 Volcano, Hawaii observed with InSAR. J. Geophys. Res. Solid Earth **117**, 1–14.
726 https://doi.org/10.1029/2011JB009123
727 Barrat, J.-A., Bachèlery, P., 2019. La Réunion Island dunites as analogs of the Martian
728 chassignites: Tracking trapped melts with incompatible trace elements. Lithos **344**,
729 452–463. https://doi.org/10.1016/j.lithos.2019.07.009
730 Battaglia, J., Aki, K., Staudacher, T., 2005. Location of tremor sources and estimation of
731 lava output using tremor source amplitude on the Piton de la Fournaise volcano: 2.
732 Estimation of lava output. J. Volcanol. Geotherm. Res. **147**, 291–308.
733 https://doi.org/10.1016/j.jvolgeores.2005.04.006
734 Berthod, C., 2016. Relation entre système intrusif et instabilités sur un volcan basaltique
735 (Piton des Neiges, La Réunion). Université de La Réunion.
736 Berthod, C., Famin, V., Bascou, J., Michon, L., Ildefonse, B., Monié, P., 2016. Evidence of
737 sheared sills related to flank destabilization in a basaltic volcano. Tectonophysics
738 **674**, 195–209. http://dx.doi.org/10.1016/j.tecto.2016.02.017

739 Blundy, J., Wood, B., 1994. Prediction of crystal–melt partition coefficients from elastic
740 moduli. Nature **372**, 452. https://doi.org/10.1038/372452a0
741 Blundy, J.D., Annen, C.J., 2016. Crustal magmatic systems from the perspective of heat
742 transfer. Elements **12**, 115–120.
743 Boudoire, G., Brugier, Y.-A., Di Muro, A., Wörner, G., Arienzo, I., Metrich, N., Zanon, V.,
744 Braukmüller, N., Kronz, A., Le Moigne, Y., 2019. Eruptive activity on the western
745 flank of Piton de la Fournaise (La Réunion Island, Indian Ocean): insights on magma
746 transfer, storage and evolution at an oceanic volcanic island. J. Petrol. **60**, 1717–
747 1752.
748 Brown, G.M., Wager, L.R., 1968. Layered igneous rocks.
749 Bureau, H., Pineau, F., Métrich, N., Semet, M.P., Javoy, M., 1998. A melt and fluid inclusion
750 study of the gas phase at Piton de la Fournaise volcano (Réunion Island). Chem.
751 Geol. **147**, 115–130. https://doi.org/10.1016/S0009-2541(97)00176-9
752 Campbell, I.H., 1977. A study of macro-rhythmic layering and cumulate processes in the
753 jimberlana intrusion, Western Australia. part I: The upper layered series. J. Petrol.
754 **18**, 183–215. https://doi.org/10.1093/petrology/18.2.183
755 Cashman, K. V, Sparks, R.S.J., Blundy, J.D., 2017. Vertically extensive and unstable
756 magmatic systems: a unified view of igneous processes. Science. **355**, eaag3055.
757 Cawthorn, R., Walraven, F., 1998. Emplacement and crystallization time for the Bushveld
758 Complex. J. Petrol. 39, 1669–1687. https://doi.org/10.1093/petrology/39.9.1669
759 Cawthorn, R.G., 2007. Cr and Sr: Keys to parental magmas and processes in the Bushveld
760 Complex, South Africa. Lithos **95**, 381–398.
761 https://doi.org/10.1016/j.lithos.2006.09.004
762 Cawthorn, R.G., 1996. Layered intrusions. Elsevier.
763 Chaput, M., Famin, V., Michon, L., 2014a. Deformation of basaltic shield volcanoes under
764 cointrusive stress permutations. J. Geophys. Res. Solid Earth **119**, 274–301.
765 https://doi.org/10.1002/2013jb010623
766 Chaput, M., Pinel, V., Famin, V., Michon, L., Froger, J.-L., 2014b. Cointrusive shear
767 displacement by sill intrusion in a detachment: A numerical approach. Geophys.
768 Res. Lett. **41**, 799–804. https://doi.org/10.1002/2013GL058813
769 Chevallier, L., Vatin-Perignon, N., 1982. Volcano-structural evolution of Piton des Neiges,
770 Reunion Island, Indian Ocean. Bull. Volcanol. 45, 285–298.
771 https://doi.org/10.1007/BF02597253

772 Chovelon, P., 1986. Forage géothermique de Salazie SLZI, Etude géologique du forage.
773 Rapport 86CFG018.
774 Coats, R.R., 1936. Primary banding in basic plutonic rocks. J. Geol. **44**, 407–419.
775 Courtillot, V., Davaille, A., Besse, J., Stock, J., 2003. Three distinct types of hotspots in the
776 Earth's mantle. Earth Planet. Sci. Lett. **205**, 295–308.
777 https://doi.org/10.1016/S0012-821X(02)01048-8
778 de Voogd, B., Pou Palomé, S., Hirn, A., Charvis, P., Gallart, J., Rousset, D., Danobeitia, J.,
779 Perroud, H., 1999. Vertical movements and material transport during hotspot
780 activity: Seismic reflection profiling offshore La Réunion. Geophys. Res. Lett. **104**,
781 2855–2874. https://doi.org/10.1029/98JB02842
782 Demange, J., Chovelon, P., Puvilland, P., 1989. Geothermal model of the Salazie Cirque
783 (Reunion Island) : Volcanic and structural implications. J. Volcanol. Geotherm. Res.
784 **36**, 153–176. https://doi.org/10.1016/0377-0273(89)90011-5
785 Deniel, C., Vidal, P., Fernandez, A., Le Fort, P., Peucat, J.-J., 1987. Isotopic study of the
786 Manaslu granite (Himalaya, Nepal): inferences on the age and source of Himalayan
787 leucogranites. Contrib. to Mineral. Petrol. **96**, 78–92.
788 Di Muro, A., Métrich, N., Vergani, D., Rosi, M., Armienti, P., Fougeroux, T., Deloule, E.,
789 Arienzo, I., Civetta, L., 2014. The shallow plumbing system of Piton de la Fournaise
790 Volcano (La Reunion Island, Indian Ocean) revealed by the major 2007 caldera-
791 forming eruption. J. Petrol. **55**, 1287–1315.
792 https://doi.org/10.1093/petrology/egu025
793 Duncan, R.A., Backman, J., Peterson, L., Party, T.S.S., 1989. Reunion hotspot activitity
794 through tertiary time: Initial results from the ocean drilling program, leg 115. J.
795 Volcanol. Geotherm. Res. **36**, 193–198. https://doi.org/10.1016/0377-
796 0273(89)90013-9
797 Edmonds, M., Cashman, K. V, Holness, M., Jackson, M., 2019. Architecture and dynamics
798 of magma reservoirs A **377**: 20180298. https://doi.org/10.1098/rsta.2018.0298
799 Famin, V., Berthod, C., Michon, L., Eychenne, J., Brothelande, E., Mahabot, M.-M., Chaput,
800 M., 2016. Localization of magma injections, hydrothermal alteration, and
801 deformation in a volcanic detachment (Piton des Neiges, La Réunion). J. Geodyn.
802 **101**, 155–169. https://doi.org/https://doi.org/10.1016/j.jog.2016.05.007
803 Famin, V., Michon, L., 2010. Volcano destabilization by magma injections in a
804 detachment. Geology **38**, 219–222. https://doi.org/10.1130/G30717.1

805 Famin, V., Welsch, B., Okumura, S., Bachèlery, P., Nakashima, S., 2009. Three
806 differentiation stages of a single magma at Piton de la Fournaise volcano (Reunion
807 hot spot). Geochemistry, Geophys. Geosystems **10**, 1–18.
808 https://doi.org/10.1029/2008GC002015
809 Fisk, M.R., Upton, B.G.J., Ford, C.E., White, W.M., 1988. Geochemical and experimental
810 study of the genesis of magmas of Réunion Island, Indian Ocean. J. Geophys. Res. **93**,
811 4933–4950. https://doi.org/10.1029/JB093iB05p04933
812 Fodor, R. V, Galar, P., 1997. A view into the subsurface of Mauna Kea volcano, Hawaii:
813 crystallization processes interpreted through the petrology and petrography of
814 gabbroic and ultramafic xenoliths. J. Petrol. **38**, 581–624.
815 https://doi.org/10.1093/petroj/38.5.581
816 Gailler, L.-S., Lénat, J.-F., Lambert, M., Levieux, G., Villeneuve, N., Froger, J.-L., 2009.
817 Gravity structure of Piton de la Fournaise volcano and inferred mass transfer
818 during the 2007 crisis. J. Volcanol. Geotherm. Res. **184**, 31–48.
819 https://doi.org/10.1016/j.jvolgeores.2009.01.024
820 Gailler, L., 2010. Structure interne d'un système volcanique océanique de type point
821 chaud: La Réunion (Océan Indien)-Approches géophysiques.
822 Gailler, L.S., Lénat, J.F., 2012. Internal architecture of La Réunion (Indian Ocean) inferred
823 from geophysical data. J. Volcanol. Geotherm. Res. **221–222**, 83–98.
824 https://doi.org/10.1016/j.jvolgeores.2012.01.015
825 Gailler, L.S., Lénat, J.F., 2010. Three-dimensional structure of the submarine flanks of La
826 Réunion inferred from geophysical data. J. Geophys. Res. Solid Earth **115**, 1–27.
827 https://doi.org/10.1029/2009JB007193
828 Gayer, E., Michon, L., Louvat, P., Gaillardet, J., 2019. Storm-induced precipitation
829 variability control of long-term erosion. Earth Planet. Sci. Lett. **517**, 61–70.
830 https://doi.org/10.1016/j.epsl.2019.04.003
831 Gillot, P.-Y., Lefèvre, J.-C., Nativel, P.-E., 1994. Model for the structural evolution of the
832 volcanoes of Réunion Island. Earth Planet. Sci. Lett. **122**, 291–302.
833 https://doi.org/10.1016/0012-821X(94)90003-5
834 Gillot, P.-Y., Nativel, P., 1982. K/Ar chronology of the ultimate activity of Piton des Neiges
835 volcano, Reunion Island, Indian Ocean. J. Volcanol. Geotherm. Res. **13**, 131–146.
836 https://doi.org/https://doi.org/10.1016/0377-0273(82)90024-5
837 Glazner, A.F., Bartley, J.M., Coleman, D.S., Gray, W., Taylor, R.Z., 2004. Are plutons

838 assembled over millions of years by amalgamation from small magma chambers?
839 GSA today **14**, 4–12.
840 Grocott, J., Arévalo, C., Welkner, D., Cruden, A., 2009. Fault-assisted vertical pluton
841 growth: Coastal Cordillera, north Chilean Andes. J. Geol. Soc. London. **166**, 295–301.
842 Gudmundsson, A., 2012. Magma chambers : Formation , local stresses , excess pressures
843 , and compartments. J. Volcanol. Geotherm. Res. **237–238**, 19–41.
844 https://doi.org/10.1016/j.jvolgeores.2012.05.015
845 Helz, R.T., Kirschenbaum, H., Marinenko, J.W., 1989. Diapiric transfer of melt in Kilauea
846 Iki lava lake, Hawaii: a quick, efficient process of igneous differentiation. Geol. Soc.
847 Am. Bull. **101**, 578–594.
848 Holness, M.B., 2005. Spatial constraints on magma chamber replenishment events from
849 textural observations of cumulates: The Rum Layered Intrusion, Scotland. J. Petrol.
850 **46**, 1585–1601. https://doi.org/10.1093/petrology/egi027
851 Hoover, J.D., 1989. Petrology of the marginal border series of the skaergaard intrusion. J.
852 Petrol. **30**, 399–439. https://doi.org/10.1093/petrology/30.2.399
853 Hunter, R.H., Sparks, R.S.J., 1987. The differentiation of the Skaergaard Intrusion.
854 Contrib. to Mineral. Petrol. **95**, 451–461. https://doi.org/10.1007/BF00402205
855 Irvine, T.N., 1982. Terminology for layered intrusions. J. Petrol. 23, 127–162.
856 Irvine, T.N., Andersen, J.C.Ø., Brooks, C.K., 1998. Included blocks (and blocks within
857 blocks) in the Skaergaard intrusion: Geologic relations and the origins of rhythmic
858 modally graded layers. Bull. Geol. Soc. Am. **110**, 1398–1447.
859 https://doi.org/10.1130/0016-7606(1998)110<1398:IBABWB>2.3.CO;2
860 Jackson, M.D., Blundy, J., Sparks, R.S.J., 2018. Chemical differentiation, cold storage and
861 remobilization of magma in the Earth's crust. Nature **564**, 405–409.
862 Jaques, A.L., 1981. Petrology and petrogenesis of cumulate peridotites and gabbros from
863 the marum ophiolite complex, Northern Papua New Guinea. J. Petrol. **22**, 1–40.
864 https://doi.org/10.1093/petrology/22.1.1
865 Jaupart, C., Tait, S., 1995. Dynamics of differentiation in magma reservoirs. J. Geophys.
866 Res. Solid Earth **100**, 17615–17636.
867 Johnson, K.T.M., 1998. Experimental determination of partition coefficients for rare
868 earth and high-field-strength elements between clinopyroxene, garnet, and basaltic
869 melt at high pressures. Contrib. to Mineral. Petrol. **133**, 60–68.
870 https://doi.org/10.1007/s004100050437

871 Karakas, O., Degruyter, W., Bachmann, O., Dufek, J., 2017. Lifetime and size of shallow
872 magma bodies controlled by crustal-scale magmatism. Nat. Geosci. **10**, 446–450.
873 Kluska, J.M., 1997. Evolution magmatique et morpho-structurale du Piton des Neiges au
874 cours des derniers 500 000 ans. Université Paris XI - Orsay.
875 Lacroix, A., 1936. Le Volcan actif de l'île de la Réunion et ses produits.[-Le volcan actif de
876 l'île de la Réunion (supplément) et celui de la Grande-Comore]. Gauthier-Villars.
877 Lacroix, A., 1923. Minéralogie de Madagascar. A. Challamel, éditeur, Librairie maritime
878 et coloniale.
879 Lacroix, A., 1916. Sur quelques roches volcaniques mélanocrates des Possessions
880 françaises de l'océan Indien et du Pacifique. Comptes Rendus **163**, 182–183.
881 Larrea, P., França, Z., Lago, M., Widom, E., Galé, C., Ubide, T., 2013. Magmatic Processes
882 and the Role of Antecrysts in the Genesis of Corvo Island (Azores Archipelago ,
883 Portugal). J. Petrol. **54**, 769–793. https://doi.org/10.1093/petrology/egs084
884 Latypov, R., Chistyakova, S., Alapieti, T., 2007. Revisiting problem of chilled margins
885 associated with marginal reversals in mafic-ultramafic intrusive bodies. Lithos **99**,
886 178–206. https://doi.org/10.1016/j.lithos.2007.05.008
887 Le Friant, A., Lebas, E., Clément, V., Boudon, G., Deplus, C., De Voogd, B., Bachelery, P.,
888 2011. A new model for the evolution of la Réunion volcanic complex from complete
889 marine geophysical surveys. Geophys. Res. Lett. **38**, 6–11.
890 https://doi.org/10.1029/2011GL047489
891 Lebas, E., Le Friant, A., Deplus, C., de Voogd, B., 2018. Understanding the Evolution of an
892 Oceanic Intraplate Volcano From Seismic Reflection Data: A New Model for La
893 Réunion, Indian Ocean. J. Geophys. Res. Solid Earth **123**, 1035–1059.
894 https://doi.org/10.1002/2017JB014959
895 Lénat, J., Gibert-Malengreau, B., Galdéano, A., 2001. A new model for the evolution of the
896 volcanic island of Reunion (Indian Ocean). J. Geophys. Res. Solid Earth **106**, 8645–
897 8663. https://doi.org/10.1029/2000JB900448
898 Lénat, J.F., Bachèlery, P., 1990. Structure and dynamics of the central zone of Piton de la
899 Fournaise volcano. Le Volcanisme la Réunion. Lénat, J.-F.(Ed.), Le volcanisme la
900 Réunion—Monographie Cent. Rech. en Volcanol. Clermont-Ferrand, Fr. 257–296.
901 Lénat, J.F., Bachèlery, P., Peltier, A., 2012. The interplay between collapse structures,
902 hydrothermal systems, and magma intrusions: The case of the central area of Piton
903 de la Fournaise volcano. Bull. Volcanol. **74**, 407–421.

https://doi.org/10.1007/s00445-011-0535-3
Lerebour, P., Rançon, J.P., Augé, T., 1989. The Grand Brûlé exploration drilling: new data on the deep framework of the Piton de la Fournaise volcano. Part 2: secondary minerals. J. Volcanol. Geotherm. Res. **36**, 129–137.
Leuthold, J., Müntener, O., Baumgartner, L.P., Putlitz, B., 2014. Petrological constraints on the recycling of mafic crystal mushes and intrusion of braided sills in the Torres del Paine mafic complex (Patagonia). J. Petrol. **55**, 917–949.
Leuthold, J., Müntener, O., Baumgartner, L.P., Putlitz, B., Ovtcharova, M., Schaltegger, U., 2012. Time resolved construction of a bimodal laccolith (Torres del Paine, Patagonia). Earth Planet. Sci. Lett. **325**, 85–92.
Loucks, R.R., 1996. A precise olivine-augite Mg-Fe-exchange geothermometer. Contr. Min. Pet. **125**, 140. https://doi.org/10.1007/s004100050211
Mahoney, J.J., Duncan, R.A., Khan, W., Gnos, E., McCormick, G.R., 2002. Cretaceous volcanic rocks of the South Tethyan suture zone, Pakistan: implications for the Réunion hotspot and Deccan Traps. Earth Planet. Sci. Lett. **203**, 295–310. https://doi.org/10.1016/S0012-821X(02)00840-3
Malengreau, B., Lénat, J.-F., Froger, J.-L., 1999. Structure of Réunion Island (Indian Ocean) inferred from the interpretation of gravity anomalies. J. Volcanol. Geotherm. Res. **88**, 131–146. https://doi.org/10.1016/S0377-0273(98)00114-0
Marsh, B.D., 2006. Dynamics of magmatic systems. Elements **2**, 287–292.
Marsh, B.D., 1996. Solidification fronts and magmatic evolution. Mineral. Mag. **60**, 5–40. https://doi.org/10.1180/minmag.1996.060.398.03
McBirney, a. R., 1995. Mechanisms of differentiation in the Skaergaard Intrusion. J. Geol. Soc. London. **152**, 421–435. https://doi.org/10.1144/gsjgs.152.3.0421
McBirney, A.R., 2009. Factors governing the textural development of Skaergaard gabbros: A review. Lithos **111**, 1–5. https://doi.org/10.1016/j.lithos.2008.09.009
McBirney, A.R., Nicolas, A., 1997. The Skaergaard Layered Series. Part II. Magmatic flow and Dynamic Layering. J. Petrol. **38**, 569–580. https://doi.org/10.1093/petroj/38.5.569
McBirney, A.R., Noyes, R.M., 1979. Crystallization and layering of the skaergaard intrusion. J. Petrol. **20**, 487–554. https://doi.org/10.1093/petrology/20.3.487
McDonough, W.F., Sun, S.-S., 1995. The composition of the Earth. Chem. Geol. **120**, 223–253. https://doi.org/10.1016/0009-2541(94)00140-4

McDougall, I., 1971. The geochronology and evolution of the young volcanic island of Réunion, Indian Ocean. Geochim. Cosmochim. Acta **35**, 261–288. https://doi.org/10.1016/0016-7037(71)90037-8

Michel, J., Baumgartner, L., Putlitz, B., Schaltegger, U., Ovtcharova, M., 2008. Incremental growth of the Patagonian Torres del Paine laccolith over 90 ky. Geology 36, 459–462.

Montgomery-Brown, E.K., Sinnett, D.K., Larson, K.M., Poland, M.P., Segall, P., Miklius, A., 2011. Spatiotemporal evolution of dike opening and decollement slip at Kilauea Volcano, Hawaii. J. Geophys. Res. Solid Earth **116**, 1–14. https://doi.org/10.1029/2010JB007762

Morgan, S., Stanik, A., Horsman, E., Tikoff, B., de Saint Blanquat, M., Habert, G., 2008. Emplacement of multiple magma sheets and wall rock deformation: Trachyte Mesa intrusion, Henry Mountains, Utah. J. Struct. Geol. 30, 491–512. https://doi.org/10.1016/j.jsg.2008.01.005

Nativel, P., 1978. Volcans de La Réunion: pétrologie, facies zéolite (Piton des Neiges) sublimes (Piton de la Fournaise). Orsay.

Nicolas, A., Boudier, F., France, L., 2009. Subsidence in magma chamber and the development of magmatic foliation in Oman ophiolite gabbros. Earth Planet. Sci. Lett. **284**, 76–87. https://doi.org/10.1016/j.epsl.2009.04.012

Norman, M., Garcia, M.O., Pietruszka, A.J., 2005. Trace-element distribution coefficients for pyroxenes, plagioclase, and olivine in evolved tholeiites from the 1955 eruption of Kilauea Volcano, Hawai'i, and petrogenesis of differentiated rift-zone lavas. Am. Mineral. **90**, 888–899. https://doi.org/10.2138/am.2005.1780

Oversby, V.M., 1972. Genetic relations among the volcanic rocks of Reunion: chemical and lead isotopic evidence. Geochim. Cosmochim. Acta **36**, 1167-1179. https://doi.org/10.1016/0016-7037(72)90097-X

Page, B.A., 1994. Late-stage evolution of Piton des Neiges volcano, La Réunion.

Pallister, J.S., Hopson, C. a., 1981. Samail Ophiolite plutonic suite: Field relations, phase variation, cryptic variation and layering, and a model of a spreading ridge magma chamber. J. Geophys. Res. **86**, 2593. https://doi.org/10.1029/JB086iB04p02593

Peltier, A., Bachèlery, P., Staudacher, T., 2009. Magma transport and storage at Piton de La Fournaise (La Réunion) between 1972 and 2007: A review of geophysical and geochemical data. J. Volcanol. Geotherm. Res. **184**, 93–108.

970 https://doi.org/10.1016/j.jvolgeores.2008.12.008
971 Peltier, A., Staudacher, T., Bachèlery, P., 2010. New behaviour of the Piton de La
972 Fournaise volcano feeding system (La Réunion Island) deduced from GPS data:
973 Influence of the 2007 Dolomieu caldera collapse. J. Volcanol. Geotherm. Res. **192**,
974 48–56. https://doi.org/10.1016/j.jvolgeores.2010.02.007
975 Peters, B.J., Day, J.M.D., Taylor, L.A., 2016. Early mantle heterogeneities in the Réunion
976 hotspot source inferred from highly siderophile elements in cumulate xenoliths.
977 Earth Planet. Sci. Lett. **448**, 150–160. https://doi.org/10.1016/j.epsl.2016.05.015
978 Pinel, V., Jaupart, C., 2000. The effect of edifice load on magma ascent beneath a volcano.
979 Philos. Trans. R. Soc. London A Math. Phys. Eng. Sci. **358**, 1515–1532.
980 https://doi.org/10.1098/rsta.2000.0601
981 Poland, M.P., Jeff Sutton, A., Gerlach, T.M., 2009. Magma degassing triggered by static
982 decompression at Kilauea Volcano, Hawai'i. Geophys. Res. Lett. **36**, 1–5.
983 https://doi.org/10.1029/2009GL039214
984 Pronost, J., 2001. Etudes des relations entre réservoirs magmatiques: un exemple à l'île
985 de La Réunion.
986 Quidelleur, X., Holt, J.W., Salvany, T., Bouquerel, H., 2010. New K-Ar ages from La
987 Montagne massif, Réunion Island (Indian Ocean), supporting two geomagnetic
988 events in the time period 2.2-2.0 Ma. Geophys. J. Int. **182**, 699–710.
989 https://doi.org/10.1111/j.1365-246X.2010.04651.x
990 Rançon, J.P., Lerebour, P., Augé, T., 1989. The Grand Brule exploration drilling: New data
991 on the deep framework of the Piton de la Fournaise volcano. Part 1:
992 Lithostratigraphic units and volcanostructural implications. J. Volcanol. Geotherm.
993 Res. **36,** 113–127. https://doi.org/10.1016/0377-0273(89)90008-5
994 Rousset, D., Lesquer, A., Bonneville, A., Lénat, J.F., 1989. Complete gravity study of Piton
995 de la Fournaise volcano, Réunion Island. J. Volcanol. Geotherm. Res. **36**, 37–52.
996 https://doi.org/10.1016/0377-0273(89)90004-8
997 Ryan, M., 1988. The mechanics and three-dimentional internal structure of acitve
998 magmatic systems: Kilauea volcan, Hawaii. J. Geophys. Res. **93**, 4213–4248.
999 https://doi.org/10.1029/JB093iB05p04213
1000 Ryan, M.P., 1987. Neutral buoyancy and the mechanical evolution of magmatic systems.
1001 No. 1. University Park, Pa.: The Geochemical Society, in: Geochem. Soc. University
1002 Park, P. (Ed.), Magmatic Processes: Physicochemical Principles; Special Publication.

pp. 259–287.

Salmonsen, L.P., Tegner, C., 2013. Crystallization sequence of the Upper Border Series of the Skaergaard Intrusion: Revised subdivision and implications for chamber-scale magma homogeneity. Contrib. to Mineral. Petrol. **165**, 1155–1171. https://doi.org/10.1007/s00410-013-0852-y

Salvany, T., Lahitte, P., Nativel, P., Gillot, P.Y., 2012. Geomorphic evolution of the Piton des Neiges volcano (Réunion Island, Indian Ocean): Competition between volcanic construction and erosion since 1.4Ma. Geomorphology **136**, 132–147. https://doi.org/10.1016/j.geomorph.2011.06.009

Scoates, J.S., Weis, D., Franssens, M., Mattielli, N., Annell, H., Frey, F.A., Nicolaysen, K., Giret, A., 2008. The Val Gabbro Plutonic Suite : A Sub-volcanic Intrusion Emplaced at the End of Flood Basalt Volcanism on the Kerguelen Archipelago. J. Petrol. **49**, 79–105. https://doi.org/10.1093/petrology/egm071

Simkin, T., 1967. Flow differentiation in the picritic sills of North Skye. Ultramafic Relat. rocks 64–70.

Smietana, M., 2011. Pétrologie, géochronologie (K–Ar) et géochimie élémentaire et isotopique (Sr, Nd, Hf, Pb) des laves anciennes de La Réunion. Implications sur la construction de l'édifice volcanique. Université de La Réunion.

Sobolev, A. V, Nikogosian, I.K., 1994. Petrology of long-lived mantle plume magmatism: Hawaii, Pacific and Reunion Island, Indian Ocean. Petrology **2**, 111–144.

Sparks, R.S.J., Annen, C., Blundy, J.D., Cashman, K. V, Rust, A.C., Jackson, M.D., 2019. Formation and dynamics of magma reservoirs. Philos. Trans. R. Soc. A **377**, 20180019.

Szymanowski, D., Wotzlaw, J.-F., Ellis, B.S., Bachmann, O., Guillong, M., von Quadt, A., 2017. Protracted near-solidus storage and pre-eruptive rejuvenation of large magma reservoirs. Nat. Geosci. **10**, 777–782.

Tait, S.R., Jaupart, C., 1996. The production of chemically stratified and adcumulate plutonic igneous rocks. Mineral. Mag. **60**, 99–114. https://doi.org/10.1180/minmag.1996.060.398.07

Tegner, C., Peter, T., Holness, M.B., Jakobsen, J.K., Lesher, C.E., 2009a. Differentiation and compaction in the Skaergaard intrusion. J. Petrol. **50**, 813–840. https://doi.org/10.1093/petrology/egp020

Tegner, C., Thy, P., Holness, M.B., Jakobsen, J.K., Lesher, C.E., 2009b. Differentiation and

compaction in the Skaergaard intrusion. J. Petrol. **50**, 813–840. https://doi.org/10.1093/petrology/egp020

Tornare, E., Pilet, S., Bussy, F., 2016. Magma Differentiation in Vertical Conduits Revealed by the Complementary Study of Plutonic and Volcanic Rocks from Fuerteventura (Canary Islands). J. Petrol. **57**, 2221–2250. https://doi.org/10.1093/petrology/egx004

Upton, B.G.J., Semet, M.P., Joron, J.L., 2000. Cumulate clasts in the Bellecombe Ash Member, Piton de la Fournaise, Réunion Island, and their bearing on cumulative processes in the petrogenesis of the Réunion lavas. J. Volcanol. Geotherm. Res. **104**, 297–318. https://doi.org/10.1016/S0377-0273(00)00212-2

Upton, B.G.J., Wadsworth, W.J., 1972. Peridotite and gabbroic rocks associated with shield-forming lavas of Réunion. Contrib. to Mineral. Petrol. **35**, 139–158. https://doi.org/10.1007/BF00370925

Upton, B.G.J., Wadsworth, W.J., 1967. A complex basalt-mugearite sill in Piton des Neiges volcano, Réunion. Am. Mineral. **52**, 1475–1492.

Upton, B.G.J., Wadsworth, W.J., 1966. The basalts of Reunion Island, Indian Ocean. Bull. Volcanol. 29, 7–23. https://doi.org/10.1007/BF02597136

Vincent, B. de Saint, 1804. Voyage dans les quatre principales iles des mers d'Afrique.

Wager, L.R., Brown, G.M., 1968. General features of the Skaregaard intrusion.

Wager, L.R., Brown, G.M., 1967. Layered igneous rocks.

Wager, L.R., Deer, W.A., 1939. Geological investigations in East Greenland, pt. 3, The petrology of the Skaergaard intrusion, Kangerdlugssuaq, East Greenland.

Walker, D., Jurewicz, S., Watson, E.B., 1988. Adcumulus dunite growth in a laboratory thermal gradient. Contrib. to Mineral. Petrol. **99**, 306–319. https://doi.org/10.1007/BF00375364

Welsch, B., Faure, F., Bachèlery, P., Famin, V., 2009. Microcrysts record transient convection at Piton de la Fournaise volcano (La Réunion hotspot). J. Petrol. **50**, 2287–2305. https://doi.org/10.1093/petrology/egp076

Wolfe, E.W., Wise, W.S., Dalrymple, G.B., 1997. The geology and petrology of Mauna Kea Volcano, Hawaii; a study of postshield volcanism (n°1557). USGPO,. https://doi.org/10.3133/pp1557

Table captions

Tab. 1 Sets of samples collected at Sites 1, 2, 3 and 4; asl: above sea level.

Tab. 2 Modal composition of samples collected at Sites 1, 2, 3 and 4. Ol: olivine, Cpx: clinopyroxene, Plg: plagioclase, Amph: amphibole, and Ox: oxides.

Tab. 3 Representative compositions for olivine at the four investigated sites.

Tab. 4 Representative compositions for clinopyroxene at the four studied sites.

Tab. 5 Representative compositions for plagioclase at the four studied sites.

Tab. 6 Representative compositions for oxides in rocks from the four investigated sites

Tab. 7 Whole-rock compositions of samples collected at Sites 1, 2, 3 and 4. L.O.I.: Loss on ignition; b.d.l.: below detection limit. Peridotite*: rock type based on hand sample descriptions.

Tab. 8 Temperatures of re-equilibration calculated with the olivine-augite Mg-Fe-exchange geothermometer of Loucks (1996). The geothermometer has a standard error of ± 6 °C.

Tab. 9 Summary of the mean characteristics of Sites 1, 2, 3 and 4

Figure captions

Fig. 1 Location maps. **a)** La Réunion Island with the massifs of Piton des Neiges (PdN) and

Piton de la Fournaise (PdF). The drill holes SLZ1 (in the cirque of Salazie) and SR1 (on the eastern flank of PdF) are indicated with yellow stars. The black rectangle indicates the studied area. **b)** Shaded relief of the cirque of Salazie. **c)** Geological map of the studied area based on our field observations, and showing the locations of the four plutonic outcrops (labeled Site 1 through 4) in the Mât River. SHI: sub-horizontal intrusion. Coordinates in UTM WGS84, zone 40S.

Fig. 2 Field characteristics observed in Sites 1, 2, 3 and 4 (see Fig. 1c for location). **a)** 2 – 2.5 cm-thick clinopyroxene- and plagioclase-rich veinlets observed in Site 1 (also observed in Site 2). **b)** Lenses of peridotites separated by mafic intrusions at Site 1 (also observed in Site 2). **c)** Overview of the outcrop in Site 2, which is crosscut and surmounted by mafic and differentiated intrusions. **d)** Example of east-dipping syn-magmatic thrust faults in Site 3. **e)** West-verging overturned folds observed in Site 3. **f)** Example of folded layering in Site 4, **g)** Layering in Site 4 through modal variations in plagioclase, olivine and clinopyroxene.

Fig. 3 Stereographic diagrams of the magmatic lineations and poles to foliation measured in Sites 3 and 4. No apparent foliation or lineation is observed at Sites 1 and 2. Stereo diagrams are equal area and lower hemisphere.

Fig. 4 Rock types sampled at Sites 1, 2, 3 and 4. N: number of samples

Fig. 5 Representative parageneses and textures of samples collected at Sites 1 and 2 (transmitted light microphotographs). **a)** Dunite from Site 1 made of anhedral grains of olivine in cumulus position, and anhedral crystals of clinopyroxene and oxides in interstitial position (sample CB4010414). **b)** Dunite from Site 2 with only olivine crystals (sample GABAMONT2). **c)** and **d)** Wehrlite samples from Sites 1 and 2, respectively, in which the olivine is euhedral and in cumulus position, and clinopyroxene is poikilitic (samples CB1010414 and GABAMONT). **e)** and **f)** Wehrlite from Site 2 made of rounded grains of olivine and euhedral, sector-zoned crystals of clinopyroxene in cumulus position, and plagioclase in interstitial position (CB4230513). **g**) and **h**) Plagioclase-wehrlites from Site 2

displaying a mesocumulate texture with euhedral olivine in cumulus position, and clinopyroxene and plagioclase in interstitial position (CB1230513). Ol: olivine, Cpx: clinopyroxene, Plg: plagioclase, Amph: amphibole and Ox: oxides.

Fig. 6 Representative parageneses and textures of samples collected at Sites 3 and 4 (transmitted-light microphotographs with crossed polars). **a)** and **b)** Olivine gabbros (samples SAL111 and CB12260513 from Sites 3 and 4, respectively), in which euhedral olivine, clinopyroxene and plagioclase show intergrowth textures. **c)** and **d)** Gabbros (samples SAL110 and CB2260513, respectively). Euhedral crystals of plagioclase and clinopyroxene **e)** and **f)** Strong magmatic fabrics, marked by elongated plagioclases in ferrogabbros (samples CB16260513 and CB2290513, respectively).

Fig. 7 Chemical composition of olivine at Sites 1, 2, 3 and 4. **a)** Fo histograms. **b)** Fo vs. CaO diagram for olivine in the layered gabbros and peridotites. See the description in the main text for populations (1), (2) and (3).

Fig. 8 Chemical compositions of clinopyroxene at Sites 1, 2, 3 and 4. **a)** Mg# histograms, **b)** Mg# vs. Cr_2O_3, and c) Mg# vs. Al_2O_3.

Fig. 9 Chemical compositions of plagioclase at Sites 1, 2, 3 and 4. a) Anorthite (An) histograms, b) Anorthite vs. K_2O.

Fig. 10 Chemical compositions of oxides at Sites 1, 2, 3 and 4. a) Cr_2O_3 vs. FeO_t, b) TiO_2 vs. Al_2O_3.

Fig. 11 Whole-rock composition of samples collected at Sites 1, 2, 3 and 4. a) MgO vs. SiO_2, Peridotite*: rock type based on hand sample descriptions. b) MgO vs. CaO. c) SiO_2 vs. CaO. d) SiO_2 vs. TiO_2. e) Chondrite-normalized REE spider diagram (McDonough and Sun, 1995). f) Th vs. Sm diagram. Purple hexagon symbols represent bulk analyses of sample from Site 3 (Pronost 2001).

Fig. 12 Composition of cumulate mineral assemblages. **a)** Average Mg# for clinopyroxene plotted against Fo olivine contents, **b)** Average Mg# for oxides plotted against Fo olivine contents, **c)** Average anorthite contents versus average Mg# for clinopyroxene, **d)** Average Mg-numbers for oxide phases versus average Mg# for clinopyroxene.

Fig 13 a) NE–SW cross section of the studied area gathering the main characteristics of each outcrop of plutonic rocks (see Fig.1c for location) and introducing our two hypotheses. The first hypothesis considers that the plutonic rocks exposed by the Mât River at Sites 1, 2, 3 and 4 correspond to different levels in the upper margin of a single magma chamber, where peridotitic layers top off gabbroic layers. In our second hypothesis, the four outcrops are parts of a multiple level magma storage feeding the volcano built by repeated injections of magma. b) Sketch of the Piton des Neiges (with vertical exaggeration of the actual topography) with the location of the four plutonic outcrops at Sites 1, 2, 3 and 4 (S1, S2, S3 and S4, respectively). We suggest that gabbroic series in Sites 3–4 belong to the magmatic system of a volcanic edifice that predated the building of Piton des Neiges (i.e. Proto-Piton des Neiges). Then, a large destabilization toward the North affected severely the magmatic system of the old volcano, and lead to a migration of the volcanic center further south for the edification of Piton des Neiges and the emplacement of peridotitic series at the Sites 1–2. EC: eruptive center. Dashed line: supposed topography of the Proto-Piton des Neiges. The presence of a high resistivity body underlying the cirque of Cilaos is revealed by geophysical data (Gailler and Lénat 2012).

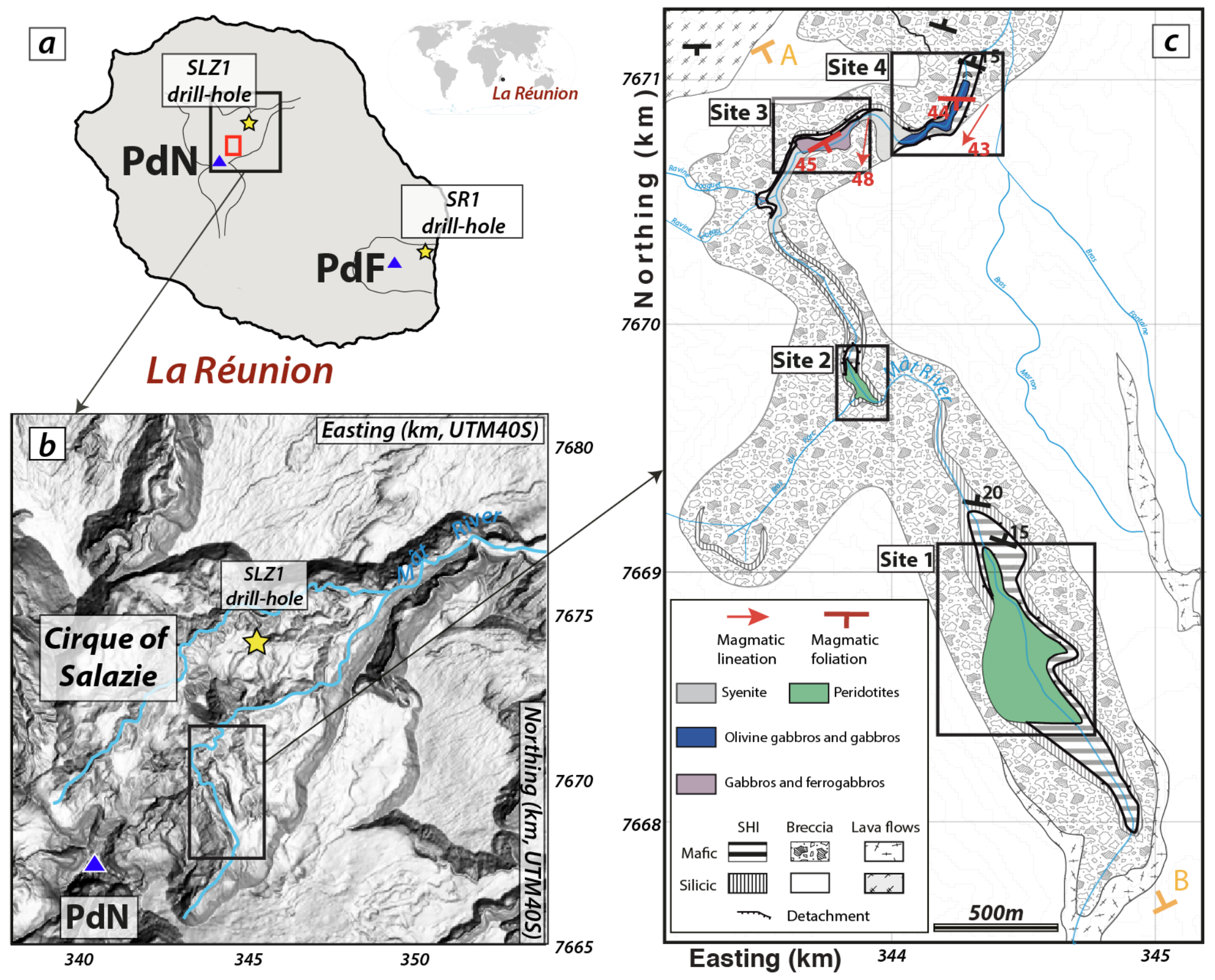
a
SLZ1
drill-hole
PdN
SR1
drill-hole
PdF
La Réunion
La Réunion
b
Easting (km, UTM40S)
SLZ1
drill-hole
Cirque of
Salazie
Mât River
PdN
Northing (km, UTM40S)
7680
7675
7670
7665
340
345
350
c
Site 4
Site 3
Site 2
Site 1
A
B
45
48
44
43
20
15
Mât River
Northing (km)
7671
7670
7669
7668
Magmatic
lineation
Magmatic
foliation
Syenite
Peridotites
Olivine gabbros and gabbros
Gabbros and ferrogabbros
SHI
Breccia
Lava flows
Mafic
Silicic
Detachment
500m
Easting (km)
344
345

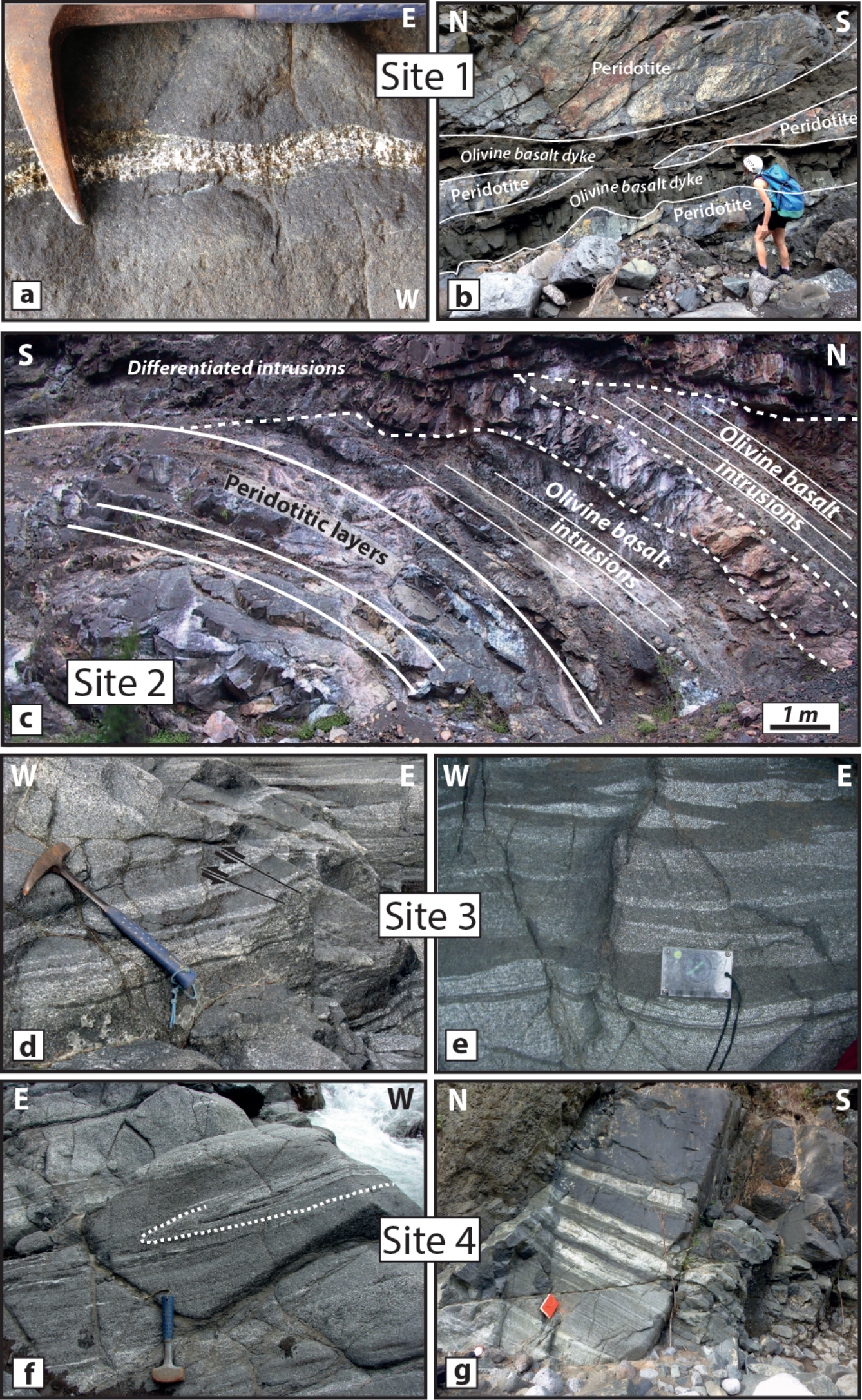
E
W
a
Site 1
N
S
Peridotite
Peridotite
Olivine basalt dyke
Peridotite
Olivine basalt dyke
Peridotite
b
S
N
Differentiated intrusions
Peridotitic layers
Olivine basalt intrusions
Olivine basalt intrusions
Site 2
c
1 m
W
E
Site 3
d
W
E
e
E
W
Site 4
f
N
S
g

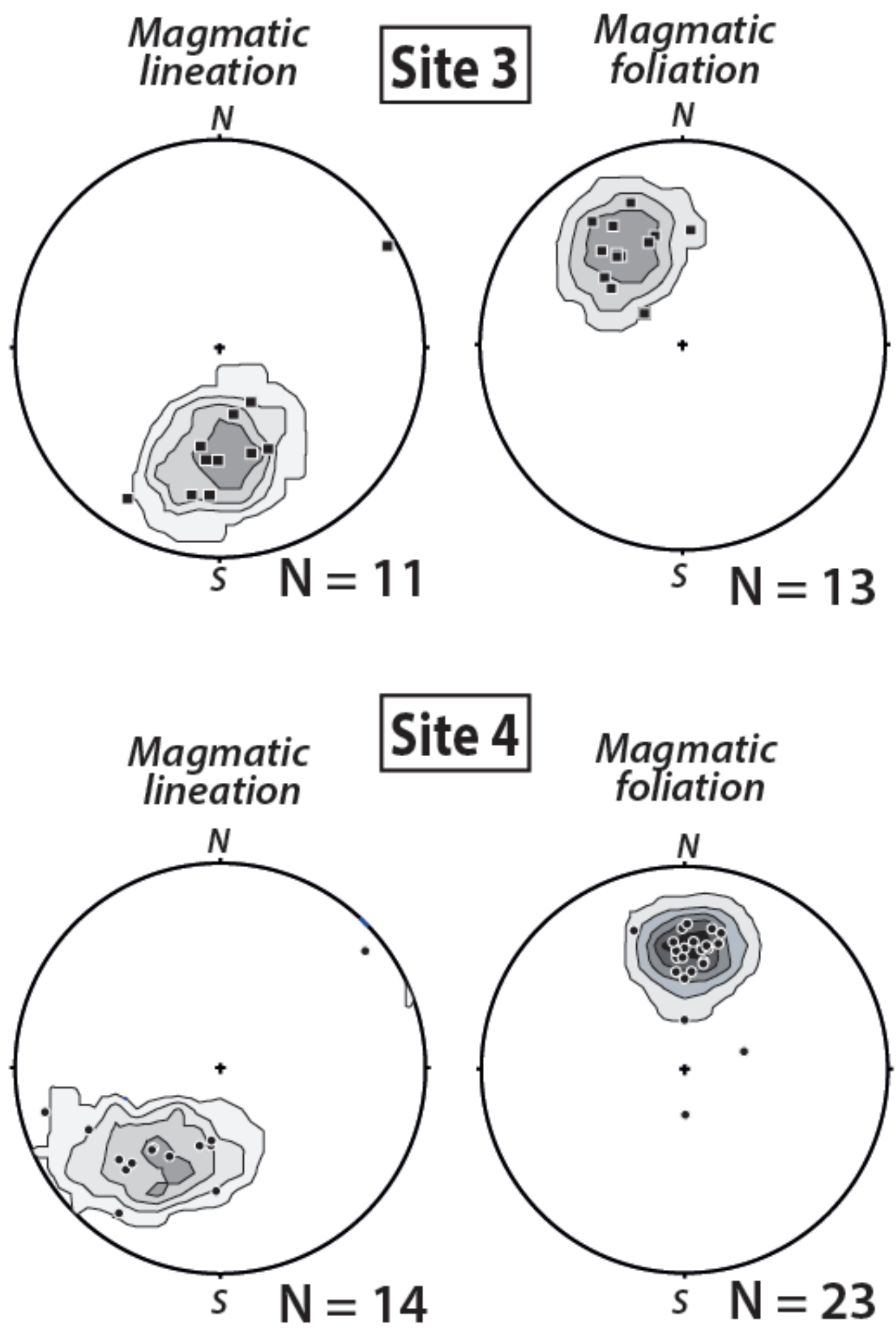
Magmatic lineation
Site 3
Magmatic foliation
N
S
N = 11
N
S
N = 13
Site 4
Magmatic lineation
Magmatic foliation
N
S
N = 14
N
S
N = 23

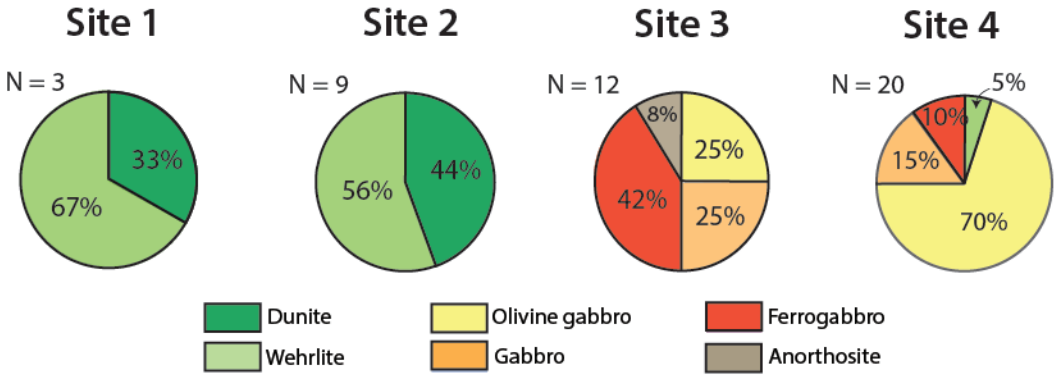
Site 1
N = 3
33%
67%
Site 2
N = 9
44%
56%
Site 3
N = 12
8%
25%
42%
25%
Site 4
N = 20
5%
10%
15%
70%
Dunite
Wehrlite
Olivine gabbro
Gabbro
Ferrogabbro
Anorthosite

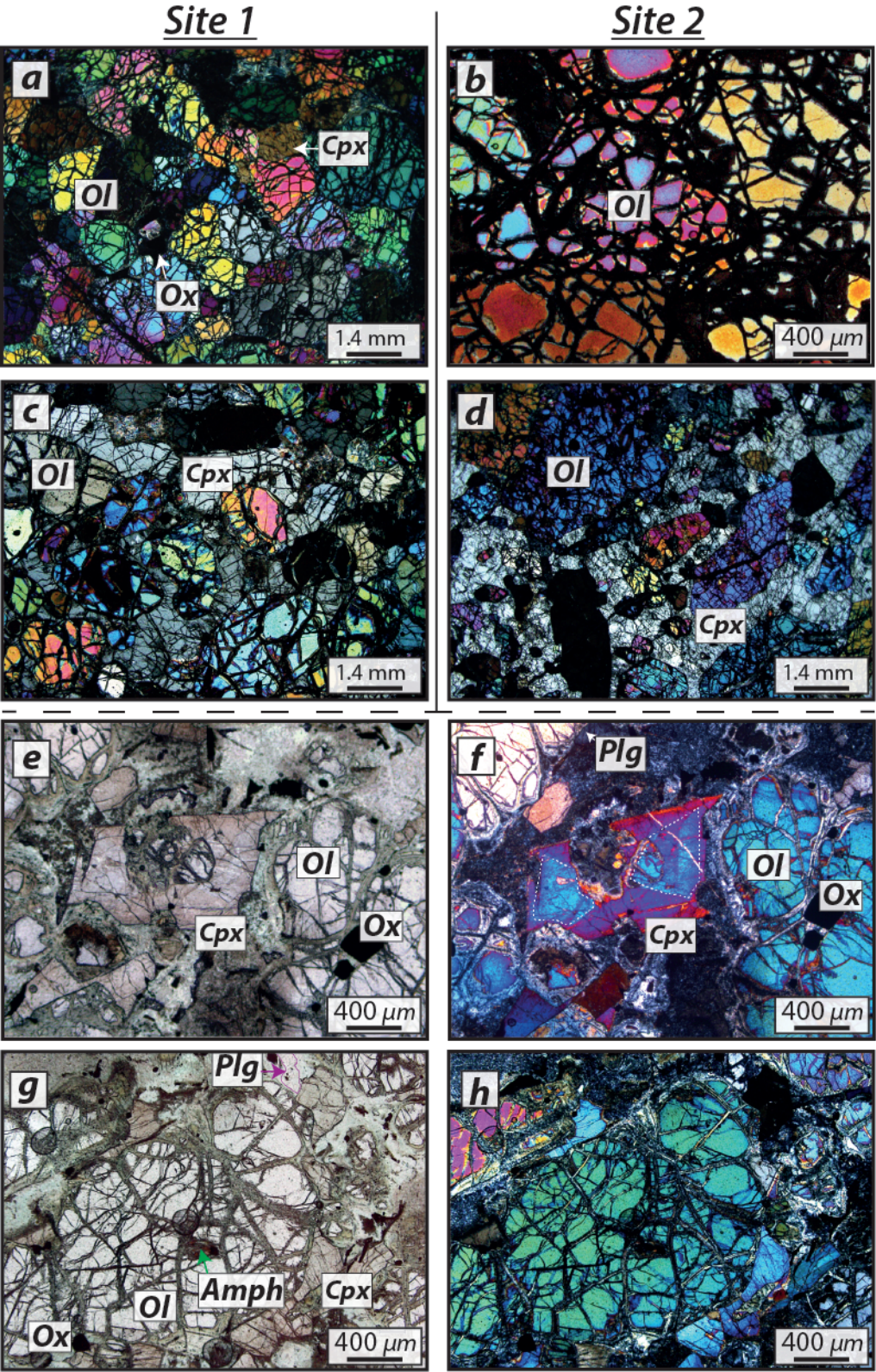
Site 1
Site 2
a
Cpx
Ol
Ox
1.4 mm
b
Ol
400 μm
c
Ol
Cpx
1.4 mm
d
Ol
Cpx
1.4 mm
e
Ol
Cpx
Ox
400 μm
f
Plg
Ol
Ox
Cpx
400 μm
g
Plg
Amph
Ol
Cpx
Ox
400 μm
h
400 μm

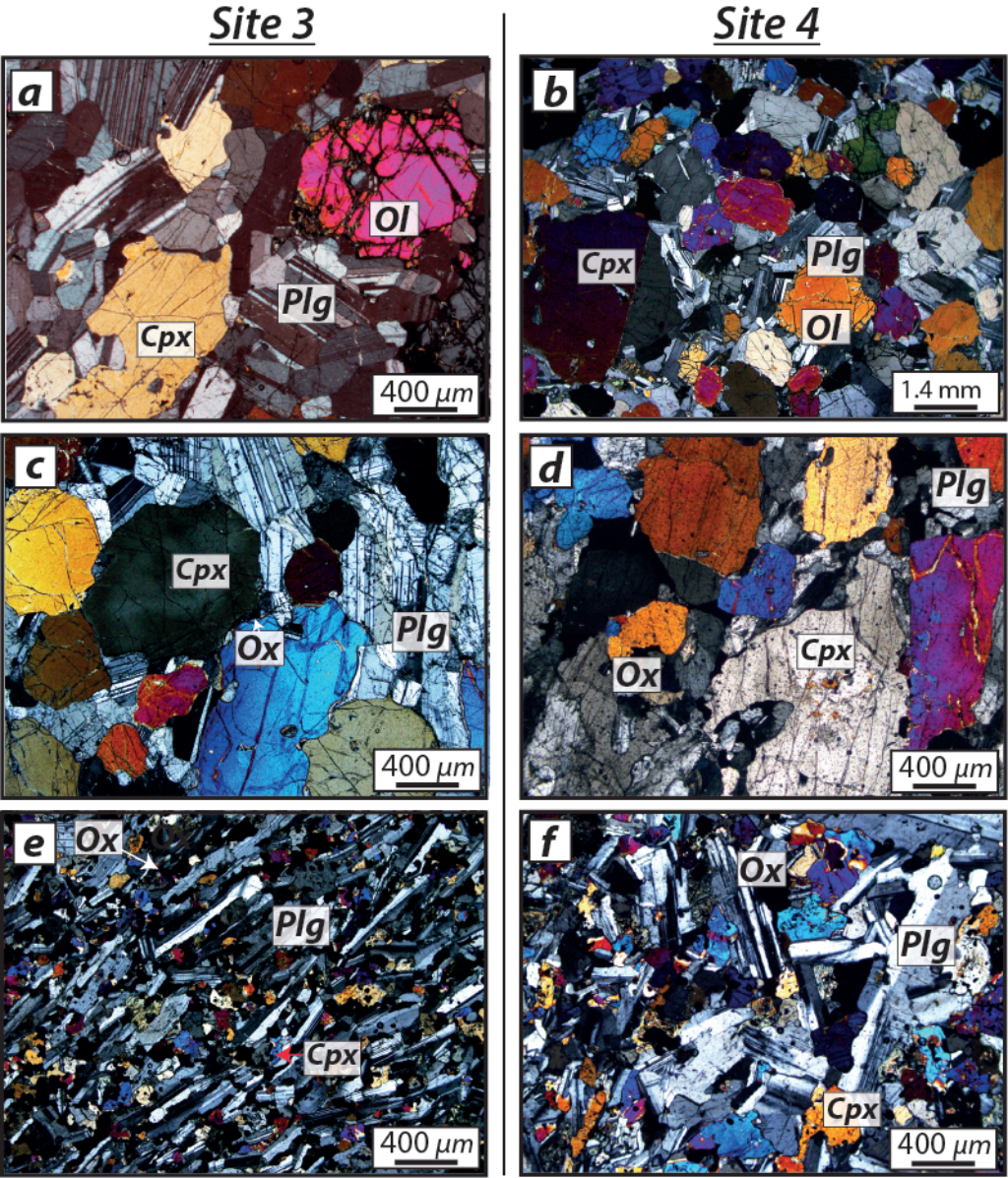
Site 3
Site 4
a
Ol
Plg
Cpx
400 μm
b
Cpx
Plg
Ol
1.4 mm
c
Cpx
Ox
Plg
400 μm
d
Plg
Ox
Cpx
400 μm
e
Ox
Plg
Cpx
400 μm
f
Ox
Plg
Cpx
400 μm

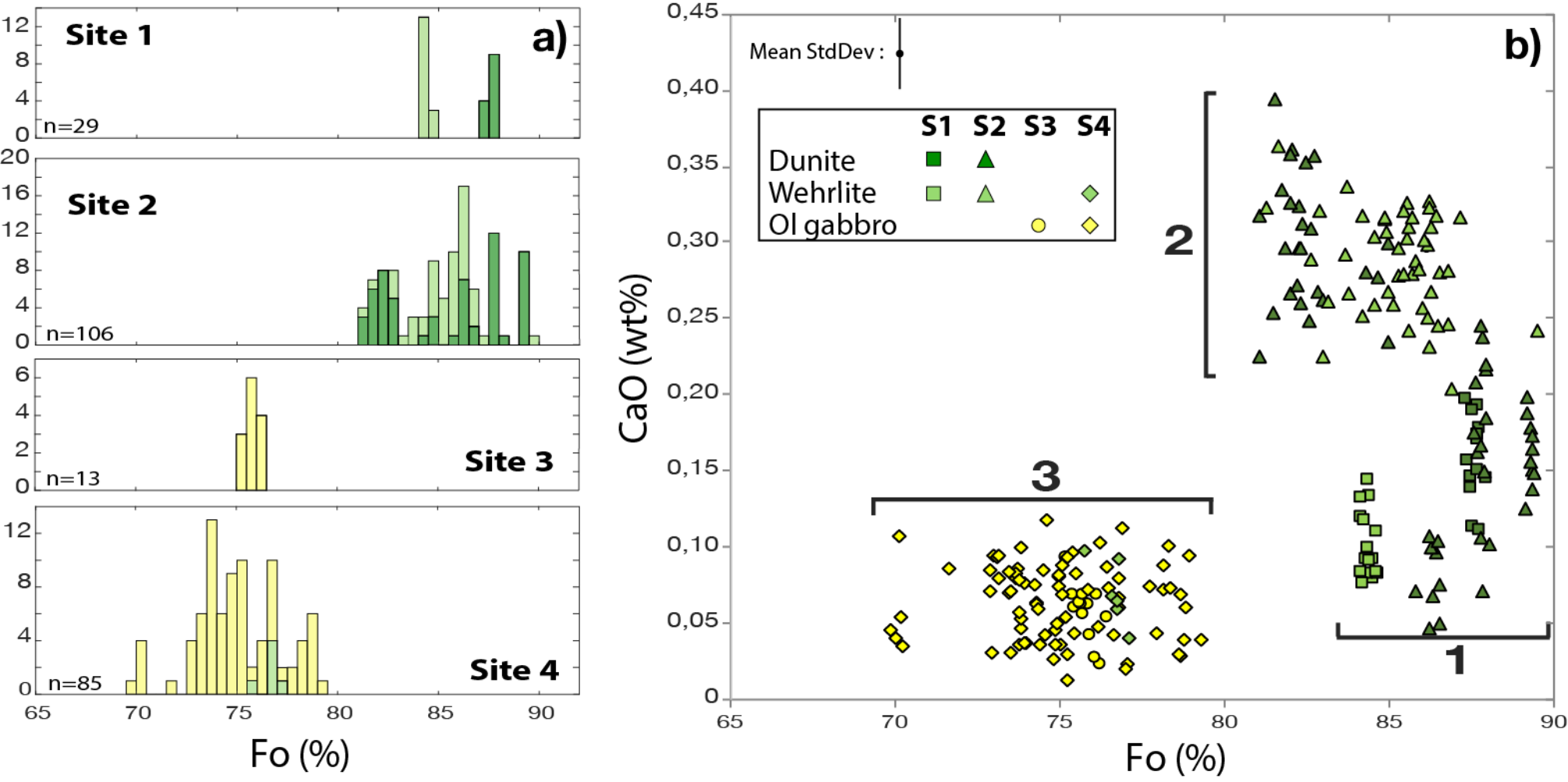
a)
Site 1
n=29
Site 2
n=106
Site 3
n=13
Site 4
n=85
Fo (%)
b)
Mean StdDev :
S1 S2 S3 S4
Dunite
Wehrlite
Ol gabbro
CaO (wt%)
Fo (%)
1
2
3

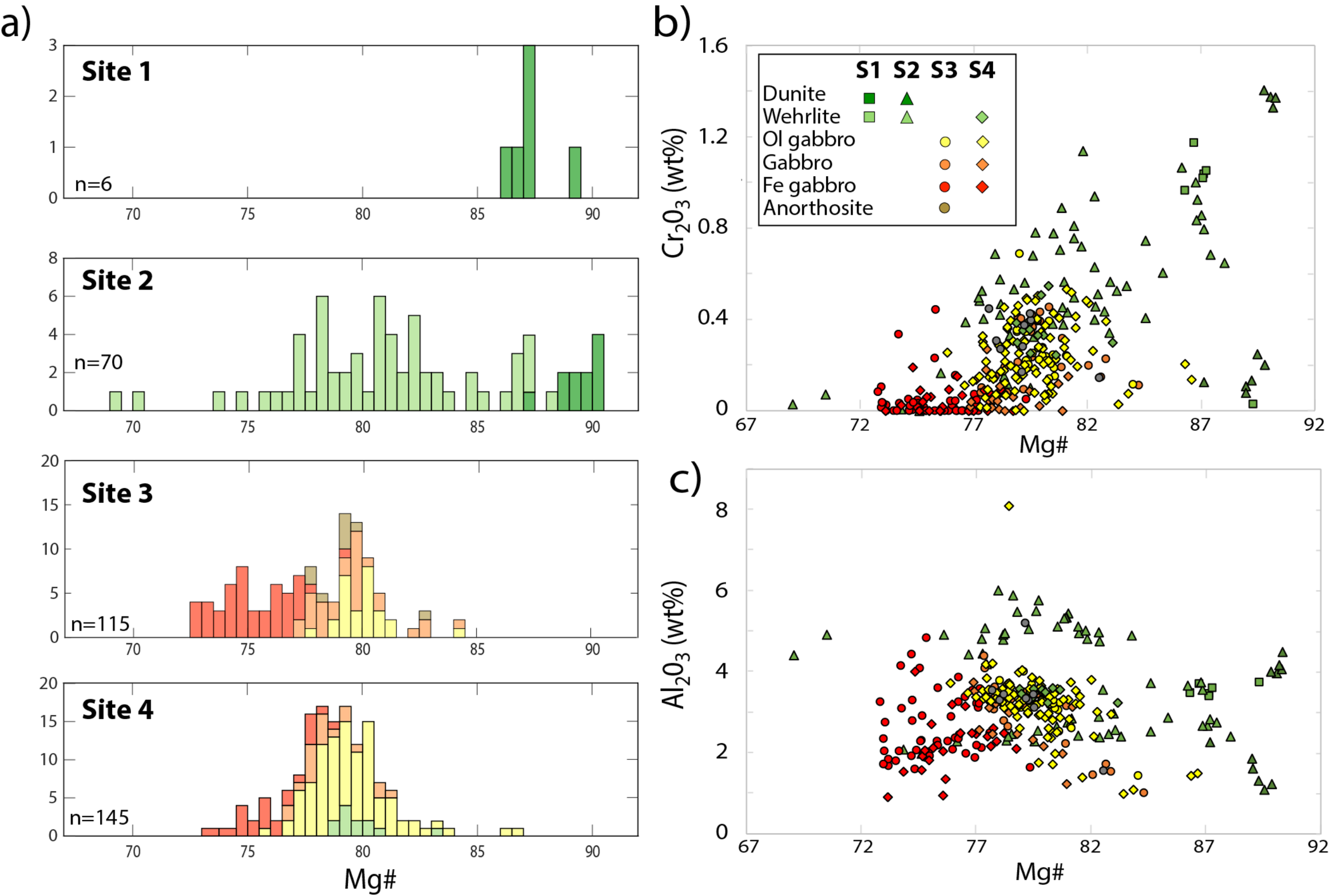
a)
Site 1
n=6
Site 2
n=70
Site 3
n=115
Site 4
n=145
Mg#
b)
S1 S2 S3 S4
Dunite
Wehrlite
Ol gabbro
Gabbro
Fe gabbro
Anorthosite
Cr2O3 (wt%)
Mg#
c)
Al2O3 (wt%)
Mg#

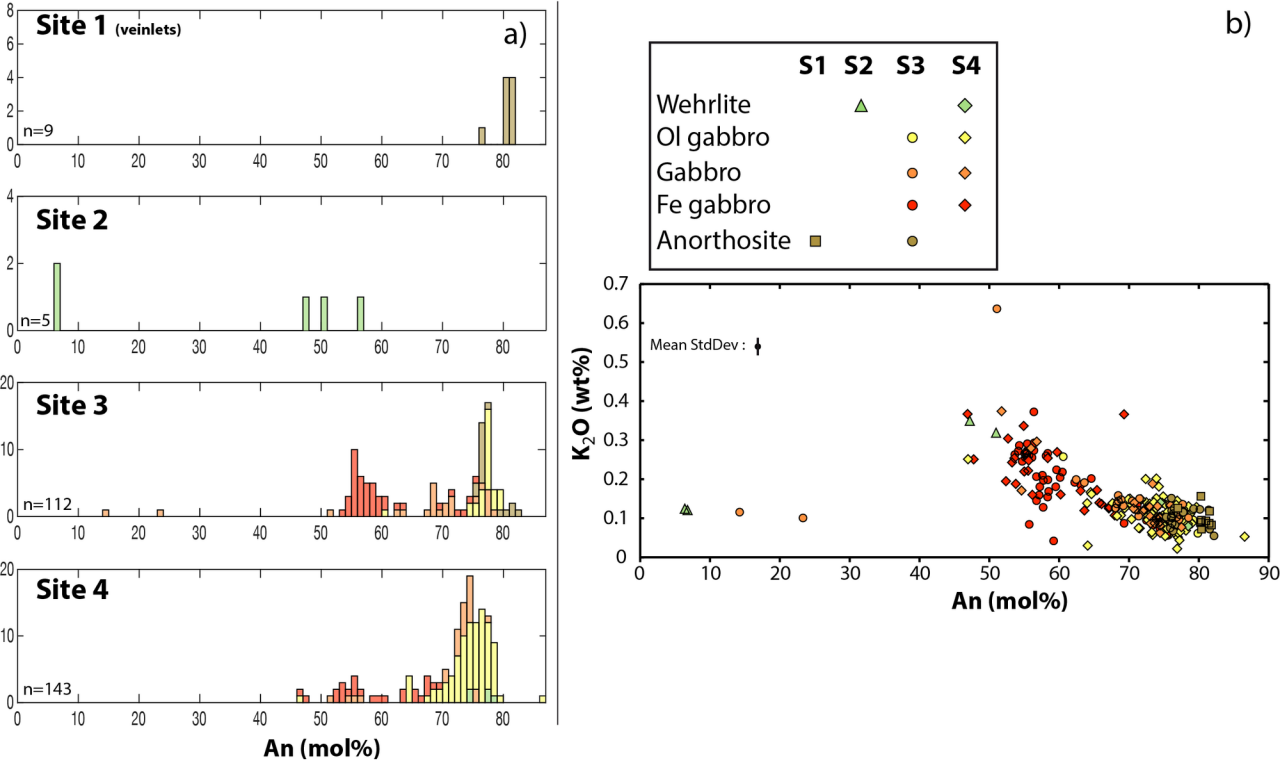
a)
Site 1 (veinlets)
n=9
Site 2
n=5
Site 3
n=112
Site 4
n=143
An (mol%)
b)
S1 S2 S3 S4
Wehrlite
Ol gabbro
Gabbro
Fe gabbro
Anorthosite
Mean StdDev :
K2O (wt%)
An (mol%)

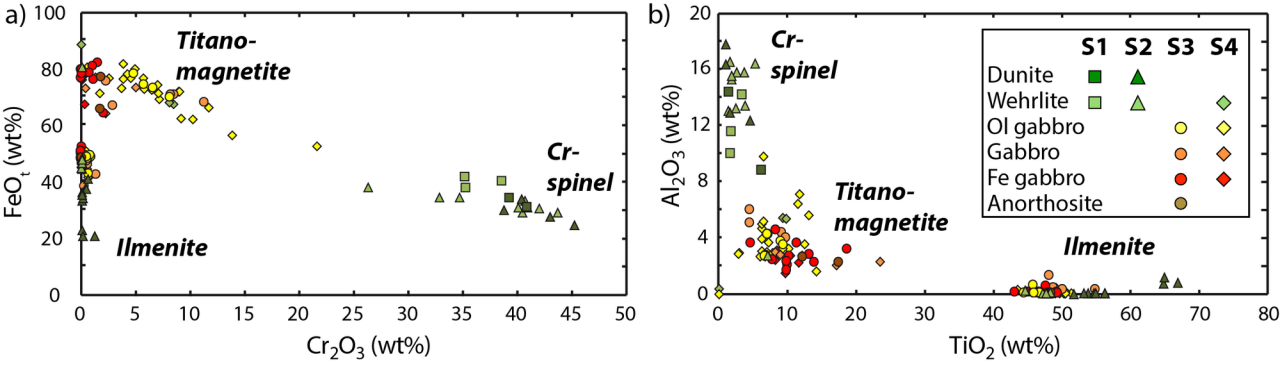
a)
Titano-
magnetite
Cr-
spinel
Ilmenite
FeO$_t$ (wt%)
Cr$_2$O$_3$ (wt%)
b)
Cr-
spinel
Titano-
magnetite
Ilmenite
S1 S2 S3 S4
Dunite
Wehrlite
Ol gabbro
Gabbro
Fe gabbro
Anorthosite
Al$_2$O$_3$ (wt%)
TiO$_2$ (wt%)

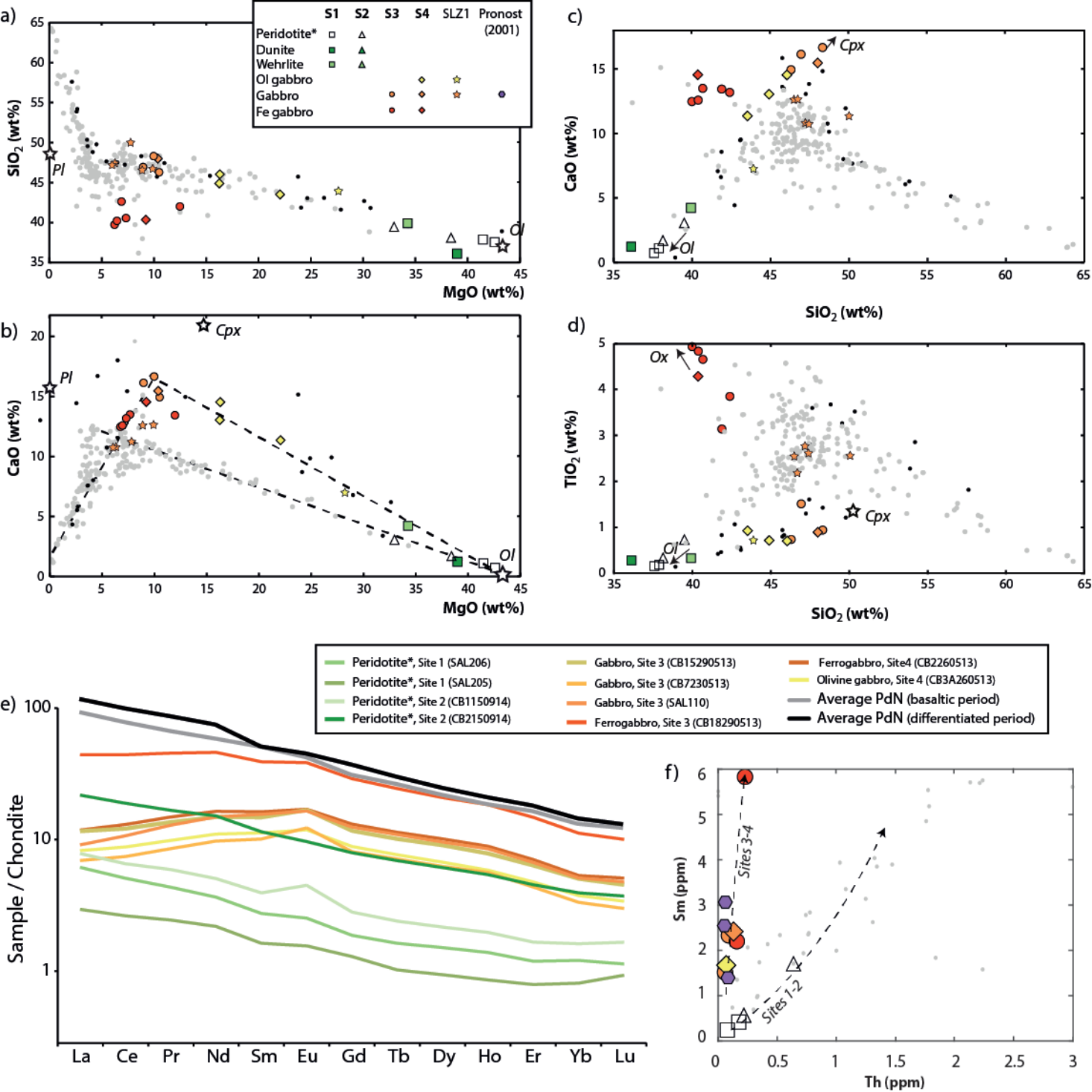
a)
S1
S2
S3
S4
SLZ1
Pronost (2001)
Peridotite*
Dunite
Wehrlite
Ol gabbro
Gabbro
Fe gabbro
SiO2 (wt%)
MgO (wt%)
Pl
Ol
b)
Cpx
Pl
Ol
CaO (wt%)
MgO (wt%)
c)
Cpx
Ol
CaO (wt%)
SiO2 (wt%)
d)
Ox
Cpx
Ol
TiO2 (wt%)
SiO2 (wt%)
Peridotite*, Site 1 (SAL206)
Peridotite*, Site 1 (SAL205)
Peridotite*, Site 2 (CB1150914)
Peridotite*, Site 2 (CB2150914)
Gabbro, Site 3 (CB15290513)
Gabbro, Site 3 (CB7230513)
Gabbro, Site 3 (SAL110)
Ferrogabbro, Site 3 (CB18290513)
Ferrogabbro, Site4 (CB2260513)
Olivine gabbro, Site 4 (CB3A260513)
Average PdN (basaltic period)
Average PdN (differentiated period)
e)
Sample / Chondite
La
Ce
Pr
Nd
Sm
Eu
Gd
Tb
Dy
Ho
Er
Yb
Lu
f)
Sm (ppm)
Th (ppm)
Sites 3-4
Sites 1-2

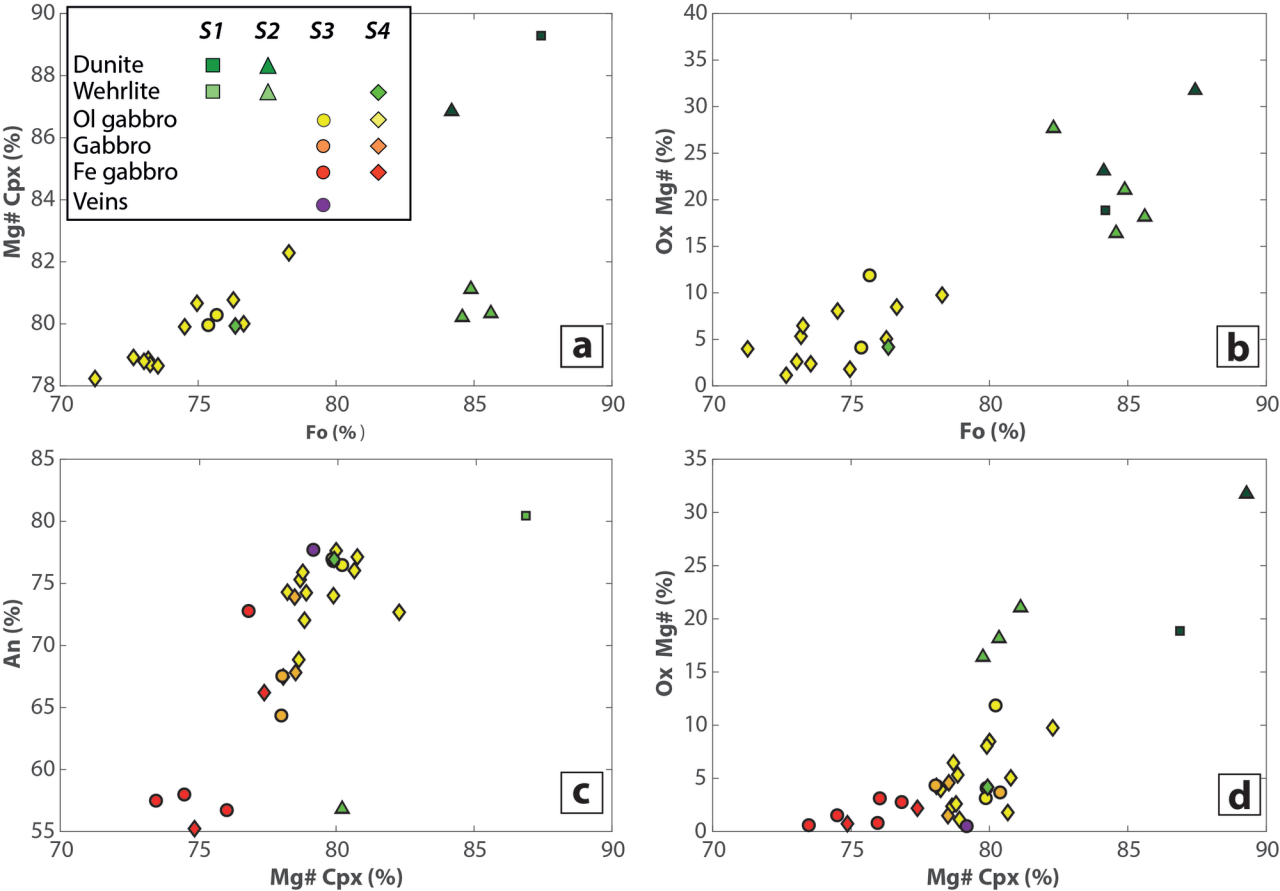
S1
S2
S3
S4
Dunite
Wehrlite
Ol gabbro
Gabbro
Fe gabbro
Veins
Mg# Cpx (%)
Fo (%)
a
Ox Mg# (%)
Fo (%)
b
An (%)
Mg# Cpx (%)
c
Ox Mg# (%)
Mg# Cpx (%)
d

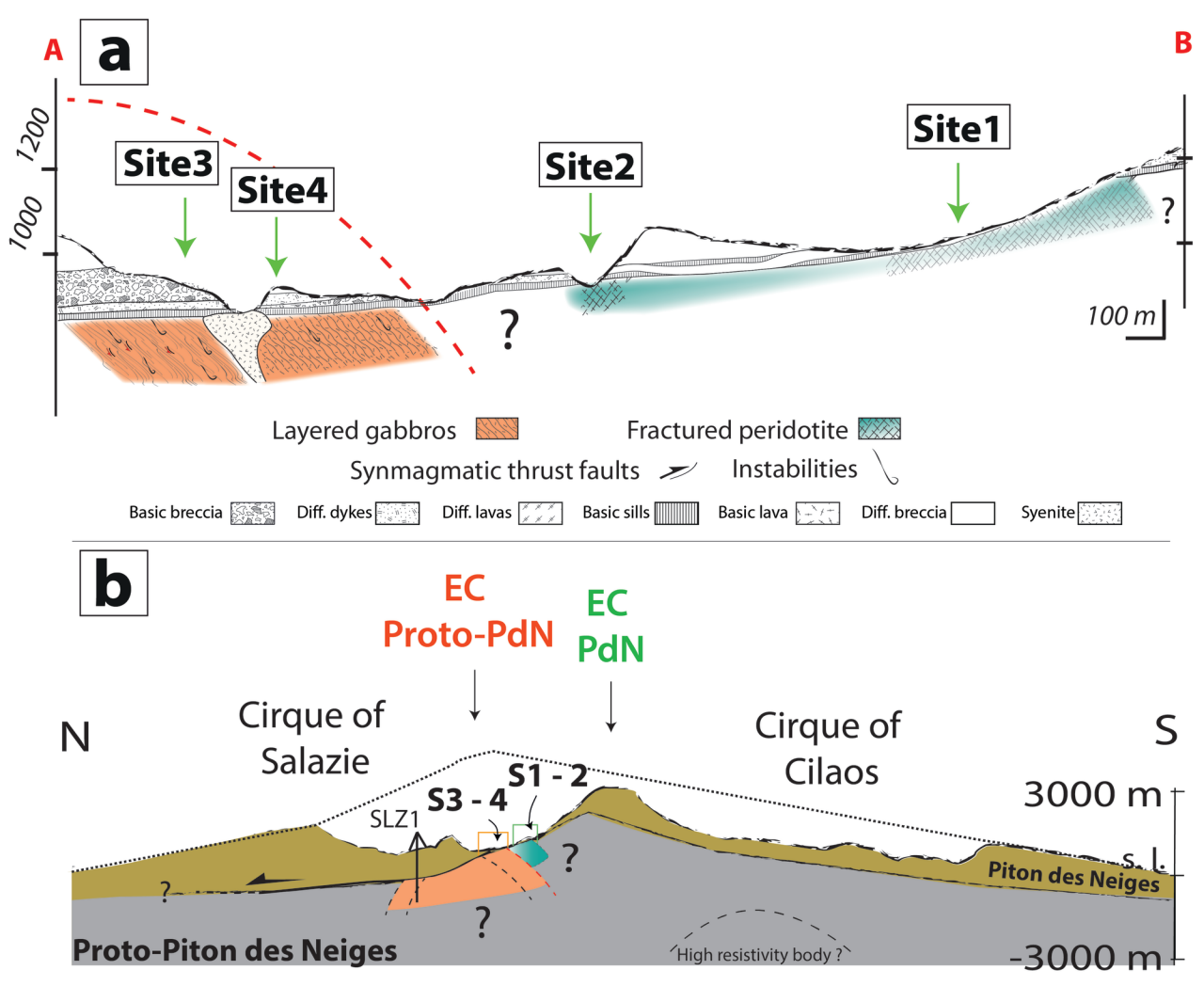
a
A
B
1200
1000
Site3
Site4
Site2
Site1
?
?
100 m
Layered gabbros
Fractured peridotite
Synmagmatic thrust faults
Instabilities
Basic breccia
Diff. dykes
Diff. lavas
Basic sills
Basic lava
Diff. breccia
Syenite
b
EC
Proto-PdN
EC
PdN
N
Cirque of
Salazie
Cirque of
Cilaos
S
S1 - 2
S3 - 4
SLZ1
3000 m
s. l.
Piton des Neiges
?
?
?
?
Proto-Piton des Neiges
High resistivity body ?
-3000 m

a)

Sites	*Structural*	*Modal composition*	*WR Majors*	*WR Traces*	*EPMA*
S1	-	3	4	2	3
S2	-	9	2	2	8
S3	24	12	8	4	12
S4	37	20	5	2	16
Total	61	44	19	10	39

b)

Sample number	Rock type	Y (UTM 40K)	X (UTM 40K)	Alt (m asl)	Thin section	WR Majors	WR Traces	EPMA
Site 1								
CB1010414	Peridotite	344518	7668658	1077	*X*	*X*		*X*
CB2010414	Peridotite	344518	7668654	1077	X			*X*
CB4010414	Peridotite	344518	7668658	1077	X	X		X
SAL205	Peridotite	344518	7668654	1077		*X*	*X*	
SAL206	Peridotite	344518	7668654	1077		*X*	*X*	
Site 2								
gabamont2	Peridotite	343808	7669828	865	X			X
gabamont1	Peridotite	343808	7669828	865	X			X
gabamont	Peridotite	343808	7669828	865	X			X
CB1150914	Peridotite	343845	7669762	882		*X*	*X*	
CB2150914	Peridotite	343808	7669712	876		*X*	*X*	
CB1230513	Peridotite	343837	7669671	920	X			X
CB2230513	Peridotite	343837	7669671	920	X			X
CB4230513	Peridotite	343837	7669671	920	X			X
CB1	Peridotite	343808	7669712	935	X			X
CB26	Peridotite	343819	7669766	872	X			
CB36	Peridotite	343808	7669840	868	*X*			*X*
Site 3								
CB15290513	Layered gabbro	343727	7670802	753	X	X	*X*	X
CB16290513	Layered gabbro	343698	7670796	755	X	*X*		X
CB17290513	Layered gabbro	343681	7670774	755	X			X
CB18290513	Layered gabbro	343649	7670780	755	X	*X*	*X*	X
CB61	Layered gabbro	343610	7670798	757	*X*			X
CB57	Layered gabbro	343677	7670781	755	*X*			X
CB55	Layered gabbro	343623	7670758	756	*X*			X
SAL110	Layered gabbro	343667	7670778	755	*X*	*X*	*X*	*X*
SAL111	Layered gabbro	343621	7670791	756	*X*			X
CB1230913	Layered gabbro	343681	7670774	755		*X*		
CB5230513	Layered gabbro	343407	7670515	860	*X*	*X*		*X*
CB6230513	Layered gabbro	343394	7670501	871	*X*	*X*		*X*
CB7230513	Layered gabbro	343446	7670547	854	*X*	*X*	*X*	*X*
Site 4								
CB1290513	Layered gabbro	344240	7670957	677	*X*			X
CB2290513	Layered gabbro	344232	7670941	678	*X*			X
CB3290513	Layered gabbro	344226	7670952	678	*X*			X
CB14260513	Layered gabbro	344193	7670877	684	*X*			
CB13260513	Layered gabbro	344197	7670891	684	*X*			X
CB12260513	Layered gabbro	344226	7670928	683	*X*	*X*		X
CB11260513	Layered gabbro	344217	7670902	684	*X*			
CB10260513	Layered gabbro	344216	7670902	684	*X*			
CB9260513	Layered gabbro	344187	7670853	685	*X*	*X*		
CB8260513	Layered gabbro	344187	7670853	685	*X*	*X*		X
CB6260513	Layered gabbro	344154	7670834	691	*X*			X
CB5260513	Layered gabbro	344154	7670833	691	*X*			X
CB4260513	Layered gabbro	344131	7670831	692	*X*			X
CB3b260513	Layered gabbro	344121	7670828	692	*X*			X
CB3a260513	Layered gabbro	344120	7670828	692	*X*	*X*	X	X
CB2260513	Layered gabbro	344106	7670815	693	*X*	*X*	X	X
CB1260513	Layered gabbro	344109	7670807	693	*X*			X
CB105	Layered gabbro	344035	7670741	708	*X*			X
CB100	Layered gabbro	343995	7670751	711	*X*			X
CB99	Layered gabbro	343973	7670766	719	*X*			X

Sample name	Rock type	Texture	Ol (vol%)	Cpx (vol%)	Plg (vol%)	Ox (vol%)	Amph (vol%)
Site 1							
CB1010414	Wehrlite	Adcumulate	70	15	10*	5	-
CB2010414	Wehrlite	Adcumulate	56	40	0	4	-
CB4010414	Dunite	Adcumulate	94	5	0	1	-
Site 2							
gabamont	Wehrlite	Heteradcumulate	80	19	0	1	-
gabamont2	Dunite	Adcumulate	100	0	0	0	-
gabamont1	Wehrlite	Heteradcumulate	70	30	< 1	0	-
CB1230513	Plg-Wehrlite	Mesocumulate	65	25	8	2	-
CB2230513	Wehrlite	Mesocumulate	60	34	4	2	-
CB4230513	Wehrlite	Mesocumulate	74	25	0	1	-
CB1	Dunite	Adcumulate	80	5	0	5	10
CB26	Dunite	Adcumulate	98	0	0	2	-
CB36	Dunite	Adcumulate	98	0	0	2	-
Site 3							
CB15290513	*Gabbro*	Mesocumulate	0	80	20	0	-
CB16290513	*Ferrogabbro*	Mesocumulate	0	35	40	25	-
CB17290513	*Ferrogabbro*	Mesocumulate	0	30	45	25	-
CB18290513	*Ferrogabbro*	Mesocumulate	0	35	40	25	-
CB61	*Ol-gabbro*	Mesocumulate	35	40	20	5	-
*CB57**	*Anorthosite*	Adcumulate	0	3	96	1	-
CB55	*Ol-gabbro*	Mesocumulate	35	40	20	5	-
SAL110	*Gabbro*	Mesocumulate	0	44	54	2	-
SAL111	*Ol-gabbro*	Mesocumulate	15	50	35	0	-
CB5230513	*Ferrogabbro*	Mesocumulate	15	25	40	20	-
CB6230513	*Ferrogabbro*	Mesocumulate	0	50	40	10	-
CB7230513	*Gabbro*	Mesocumulate	0	60	40	< 1	-
Site 4							
CB1290513	Wehrlite	Adcumulate	55	33	5	7	-
CB2290513	*Ferrogabbro*	Mesocumulate	0	50	43	7	-
CB3290513	*Ol-gabbro*	Mesocumulate	34	50	15	1	-
CB14260513	*Ol-gabbro*	Mesocumulate	15	45	39	1	-
CB13260513	*Ol-gabbro*	Mesocumulate	10	49	40	1	-
CB12260513	*Ol-gabbro*	Mesocumulate	15	50	35	0	-
CB11260513	*Ol-gabbro*	Mesocumulate	2	55	40	3	-
CB10260513	*Ol-gabbro*	Mesocumulate	35	49.5	15	0.5	-
CB9260513	*Gabbro*	Adcumulate	0	59	40	1	-
CB8260513	*Ol-gabbro*	Adcumulate to mesocumulate	34	40	25	1	-
CB6260513	*Ol-gabbro*	Mesocumulate	28	55	15	2	-
CB5260513	*Ol-gabbro*	Mesocumulate	10	40	49	1	-
CB4260513	*Ol-gabbro*	Mesocumulate	15	40	45	0	-
CB3b260513	*Ol-gabbro*	Mesocumulate	45	39	15	1	-
CB3a260513	*Ol-gabbro*	Mesocumulate	25	45	30	0	-
CB2260513	*Gabbro*	Mesocumulate	0	45	50	5	-
CB1260513	*Ferrogabbro*	Mesocumulate	0	30	45	25	-
CB105	*Gabbro*	Mesocumulate	0	54	45	1	-
CB100	*Ol-gabbro*	Mesocumulate	10	50	40	0	-
CB99	*Ol-gabbro*	Mesocumulate	20	50	30	0	-

* Vein

Rock type	Dunite		Wehrlite		Olivine gabbro	
Site	***S1***	***S2***	***S1***	***S4***	***S3***	***S4***
Sample	*CB4010414*	*Gabamont2*	*CB1010414*	*CB1290513*	*CB55*	*CB3B260513*
	Olivine	Olivine	Olivine	Olivine	Olivine	Olivine
SiO2	40.04	40.48	39.46	39.12	38.31	38.97
TiO2	0.01	0.06	0.06	0.00	0.00	0.00
Al2O3	0.04	0.03	0.01	0.03	0.04	0.02
Cr2O3	0.04	0.00	0.04	0.04	0.01	0.03
FeOt	11.48	11.13	14.43	20.70	22.11	19.50
MnO	0.26	0.16	0.18	0.29	0.34	0.33
MgO	47.72	46.90	44.80	39.37	38.51	40.71
CaO	0.15	0.22	0.08	0.04	0.06	0.04
Na2O	0.00	0.00	0.00	0.00	0.00	0.00
K2O	0.00	0.00	0.00	0.00	0.00	0.00
NiO	–	0.41	–	0.20	–	0.23
Total	99.74	99.38	99.07	99.80	99.38	99.84
Fo (mol%)	87.9	88.0	84.6	77.1	75.6	78.8

Rock type	Wehrlite		Olivine gabbro		Gabbro		Ferrogabbro		Anorthosite
Site	***S1***	***S2***	***S3***	***S4***	***S3***	***S4***	***S3***	***S4***	***S3***
Sample	*CB1010414*	*CB1230513*	*SAL111*	*CB12260513*	*SAL110*	*CB2260513*	*CB18290513*	*CB1260513*	*CB57*
	Clinopyroxene	Clinopyroxene	Clinopyroxene	Clinopyroxene	Clinopyroxene	Clinopyroxene	Clinopyroxene	Clinopyroxene	Clinopyroxene
SiO2	51.19	51.80	50.84	50.32	50.69	53.12	52.04	52.53	50.73
TiO2	1.12	0.90	1.40	1.32	1.42	0.26	0.71	0.54	1.49
Al2O3	3.58	2.55	3.28	3.77	2.76	1.20	1.96	1.51	3.27
Cr2O3	1.05	0.57	0.24	0.48	0.08	0.00	0.00	0.03	0.37
FeOt	4.26	5.93	6.79	6.80	7.29	6.49	8.16	9.29	7.00
MnO	0.14	0.14	0.15	0.12	0.19	0.24	0.40	0.31	0.12
MgO	16.34	16.25	15.25	14.98	14.64	15.43	14.93	14.70	14.99
CaO	21.88	21.12	21.58	21.57	21.74	23.01	21.63	20.92	22.08
Na2O	0.29	0.21	0.30	0.37	0.38	0.21	0.36	0.32	0.38
K2O	0.00	0.00	0.01	0.01	0.00	0.00	0.00	0.02	0.00
NiO	–	0.04	0.03	0.04	0.04	0.00	0.00	0.00	–
Total	99.85	99.51	99.85	99.79	99.23	99.96	100.21	100.17	100.42
Wo (%)	45.5	43.6	44.8	45.1	45.3	46.3	44.1	42.8	45.5
En (%)	47.3	46.6	44.0	43.6	42.5	43.2	42.3	41.9	43.0
Fs (%)	6.9	9.5	11.0	11.1	11.9	10.2	13.0	14.8	11.3
Mg#	87.2	83.0	80.0	79.7	78.2	80.9	76.5	73.8	79.3

Rock type	Wehrlite		Olivine gabbro		Gabbro		Ferrogabbro		Anorthosite
Site	***S1***	***S2***	***S3***	***S4***	***S3***	***S4***	***S3***	***S4***	***S3***
Sample	*CB1010414*	*CB1230513*	*SAL111*	*CB12260513*	*SAL110*	*CB2260513*	*CB16290513*	*CB1260513*	*CB57*
	Plagioclase	Plagioclase	Plagioclase	Plagioclase	Plagioclase	Plagioclase	Plagioclase	Plagioclase	Plagioclase
SiO2	48.41	54.04	48.88	48.17	50.57	50.22	54.40	54.08	48.28
TiO2	0.05	0.11	0.08	0.08	0.00	0.02	0.02	0.09	0.12
Al2O3	31.90	27.73	32.17	32.43	30.51	30.89	28.67	28.34	32.22
Cr2O3	0.01	0.00	0.00	0.03	0.00	0.00	0.01	0.00	0.00
FeOt	0.37	0.73	0.43	0.38	0.43	0.34	0.33	0.54	0.46
MnO	0.02	0.04	0.00	0.03	0.00	0.02	0.00	0.00	0.03
MgO	0.06	0.12	0.04	0.05	0.04	0.02	0.02	0.03	0.03
CaO	15.52	11.62	15.54	16.12	14.14	14.39	11.27	11.64	16.40
Na2O	2.48	4.68	2.61	2.35	3.43	3.22	4.90	5.00	2.29
K2O	0.13	0.29	0.11	0.13	0.15	0.13	0.26	0.22	0.12
Total	98.95	99.83	99.87	99.79	99.27	99.25	99.92	99.96	99.96
An (mol%)	77.0	56.8	76.2	78.5	68.9	70.6	55.2	55.6	79.3

Rock type	Dunite		Wehrlite				Olivine gabbro			
Site	***S1***	***S2***	***S1***	***S2***	***S4***	***S4***	***S3***	***S3***	***S4***	***S4***
Sample	*CB4010414*	*CB36*	*CB1010414*	*CB1230513*	*CB1290513*	*CB1290513*	*SAL111*	*SAL111*	*CB13260513*	*CB13260513*
Phase	Cr-Spinel	Cr-Spinel	Cr-Spinel	Cr-Spinel	Magnetite	Ti-Magnetite	Ti-Magnetite	Ilmenite	Ti-Magnetite	Ilmenite
SiO2	0.00	0.00	0.02	0.03	0.79	0.00	0.03	0.04	0.03	0.00
TiO2	6.27	1.09	1.88	2.46	0.06	9.31	7.18	48.14	7.26	50.23
Al2O3	8.77	16.35	11.51	13.21	0.34	5.45	4.23	0.06	3.64	0.09
Cr2O3	39.30	45.24	35.23	41.98	0.02	8.43	8.17	0.65	4.50	0.19
FeOt	34.11	24.64	41.70	30.51	88.65	67.57	69.88	42.72	76.64	45.49
MnO	0.33	0.25	0.40	0.24	0.04	0.42	0.25	0.56	0.29	0.91
MgO	8.79	10.61	5.73	10.10	0.68	2.67	2.84	4.83	1.53	1.41
CaO	0.00	0.01	0.00	0.00	0.30	0.04	0.00	0.38	0.00	0.00
Na2O	0.00	0.06	0.01	0.00	0.00	0.00	0.02	0.00	0.00	0.00
K2O	0.03	–	0.02	0.01	0.00	0.00	0.00	0.01	0.00	0.01
NiO	–	–	–	0.23	0.20	0.19	0.11	0.10	0.13	0.07
Total	97.60	98.25	96.49	98.77	91.09	94.06	92.72	97.50	94.03	98.39
Mg # (%)	31.5	43.4	19.7	37.1	1.3	6.6	6.8	16.8	3.4	5.2

Rock type	Gabbro				Ferrogabbro				Anorthosite	
Site	S3	S3	S4	S4	S3	S3	S4	S4	S3	S3
Sample	*SAL110*	*SAL110*	*CB2260513*	*CB2260513*	*CB16290513*	*CB16290513*	*CB1260513*	*CB1260513*	*CB57*	*CB57*
Phase	Ti-Magnetite	Ilmenite	Ti-Magnetite	Ilmenite	Ti-Magnetite	Ilmenite	Ti-Magnetite	Ilmenite	Ti-Magnetite	Ilmenite
SiO2	0.04	0.04	0.03	0.00	0.07	0.01	0.05	0.00	0.0	0.05
TiO2	9.90	46.68	9.01	48.69	13.99	47.48	11.71	48.05	12.3	48.43
Al2O3	4.00	0.14	2.81	0.10	2.27	0.13	2.26	0.30	2.6	0.03
Cr2O3	2.31	0.26	1.27	0.00	0.06	0.06	0.10	0.00	1.8	0.10
FeOt	75.57	48.86	76.85	47.53	76.40	49.58	75.94	48.10	76.9	48.42
MnO	0.32	1.22	0.41	0.70	0.50	1.09	0.50	1.42	0.4	1.59
MgO	0.80	0.34	0.46	1.37	0.30	0.24	0.17	0.16	0.2	0.15
CaO	0.08	0.28	0.20	0.02	0.16	0.04	0.11	0.06	0.1	0.21
Na2O	0.00	0.00	0.02	0.00	0.01	0.04	0.00	0.00	0.0	0.02
K2O	0.01	0.00	0.00	0.00	0.00	0.00	0.00	0.00	0.0	0.02
NiO	0.15	0.01	0.06	0.01	0.00	0.04	0.10	0.00	–	–
Total	93.19	97.83	91.13	98.42	93.76	98.70	90.95	98.09	94.4	99.02
Mg#	1.9	1.2	1.1	4.9	0.7	0.9	0.4	0.6	0.4	0.6

	Site 1				***Site 2***		***Site 3***								***Site 4***				
Rock type	Dunite	Werlhite	Peridotite*	Peridotite*	Peridotite*	Peridotite*	Fe-gabbro	Gabbro	Fe-gabbro	Fe-gabbro	Gabbro	Fe-gabbro	Fe-gabbro	Gabbro	Ol-gabbro	Ol-gabbro	Ol-gabbro	Gabbro	Fe-gabbro
Sample	*CB4010414*	*CB1010414*	*SAL206*	*SAL205*	*CB1150914*	*CB2150914*	*CB16290513*	*CB15290513*	*CB1230914*	*CB18290513*	*SAL110*	*CB5230513*	*CB6230513*	*CB7230513*	*CB12260513*	*CB3A260513*	*CB8260513*	*CB9260513*	*CB2260513*
(wt%)																			
SiO2	36.11	39.92	37.88	37.57	38.13	39.49	39.98	48.31	42.39	40.38	46.94	40.67	41.88	46.30	46.04	44.90	43.52	48.00	40.36
Al2O3	1.14	4.02	1.38	0.68	2.67	3.64	12.80	14.12	13.562	12.81	14.57	12.91	10.66	15.96	10.72	10.92	5.54	13.45	10.93
Fe2O3	10.67	12.30	11.35	12.36	11.28	13.64	18.36	6.38	15.875	18.90	8.38	18.02	16.41	6.73	9.18	10.12	14.87	6.03	18.18
MnO	0.14	0.16	0.15	0.16	0.15	0.18	0.25	0.11	0.2027	0.24	0.12	0.24	0.20	0.10	0.14	0.15	0.20	0.10	0.18
MgO	38.99	34.26	41.47	42.58	38.41	32.96	6.75	9.97	7.303	6.94	8.96	7.66	11.96	10.49	16.30	16.25	22.06	10.37	9.22
CaO	1.23	4.23	1.11	0.72	1.72	3.07	12.48	16.66	13.183	12.58	16.14	13.50	13.44	14.94	14.54	13.04	11.36	15.47	14.55
Na2O	0.05	0.44	0.05	0.01	0.06	0.27	1.94	1.69	2.051	2.05	1.65	1.67	0.87	1.29	0.81	0.87	0.41	1.75	1.05
K2O	0.04	0.04	0.04	0.01	0.07	0.15	0.11	0.37	0.163	0.11	0.20	0.10	0.06	0.60	0.11	0.09	0.03	0.51	0.09
TiO2	0.28	0.33	0.18	0.16	0.34	0.74	4.93	0.94	3.849	4.83	1.51	4.65	3.14	0.74	0.70	0.72	0.93	0.89	4.28
P2O5	0.05	0.04	0.04	0.04	0.04	0.10	0.80	b.d.l.	0.34	0.47	b.d.l.	0.61	b.d.l.	b.d.l.	b.d.l.	b.d.l.	b.d.l.	b.d.l.	b.d.l.
L.O.I.	9.84	4.60	5.19	4.50	6.52	4.68	0.37	1.76	0.86	0.85	1.28	0.63	2.06	2.73	1.17	1.47	1.29	2.25	0.53
Total	98.54	100.34	98.84	98.79	99.39	98.91	98.77	100.31	99.77	100.15	99.75	100.64	100.67	99.88	99.71	98.53	100.20	98.82	99.36
(p.p.m.)																			
La			1.47	0.70	1.87	5.19		2.76		10.53	2.17			1.65		1.96			2.81
Ce			3.13	1.62	4.04	11.64		7.46		27.22	6.58			4.58		5.42			8.02
Pr			0.41	0.23	0.55	1.56		1.27		4.24	1.20			0.80		0.92			1.39
Nd			1.68	1.00	2.32	6.95		6.82		21.15	6.84			4.48		5.06			7.54
Sm			0.41	0.24	0.59	1.71		2.20		5.81	2.32			1.50		1.67			2.42
Eu			0.14	0.09	0.25	0.55		0.95		2.17	0.93			0.70		0.67			0.96
Gd			0.37	0.26	0.56	1.59		2.33		5.81	2.49			1.62		1.77			2.62
Tb			0.06	0.04	0.09	0.25		0.37		0.89	0.40			0.26		0.28			0.41
Dy			0.37	0.23	0.53	1.51		2.24		5.16	2.37			1.54		1.66			2.50
Ho			0.08	0.05	0.11	0.30		0.43		1.01	0.47			0.31		0.32			0.49
Er			0.19	0.13	0.27	0.73		1.02		2.37	1.08			0.70		0.77			1.13
Yb			0.20	0.13	0.26	0.64		0.82		1.81	0.83			0.54		0.61			0.86
Lu			0.03	0.02	0.04	0.09		0.11		0.25	0.12			0.07		0.08			0.13
Th			0.18	0.08	0.22	0.64		0.16		0.23	0.09			0.06		0.07			0.13
Sc			7.27	6.22	8.26	13.53		56.59		35.75	50.64			48.62		43.28			55.34
Ni			2112	2215	2016	1415		201		48	141			224		421			164

Sample	Rock type	$(Fe/Mg)_{cpx}$	$(Fe/Mg)_{ol}$	$K_D^{(Ol/Aug)}$	T (°C)
Site 1					
CB1010414	*Wehrlite*	0.129	0.177	1.371	1165
Site 2					
CB4230513 [#]	*Wehrlite*	0.178	0.171	0.960	1275
CB2230513 [#]	*Wehrlite*	0.182	0.160	0.880	1278
CB1230513 [#]	*Wehrlite*	0.203	0.175	0.861	1279
CB1	*Dunite*	0.103	0.157	1.526	1130
Site 3					
SAL111	*Ol-gabbro*	0.199	0.315	1.584	1118
CB55	*Ol-gabbro*	0.192	0.320	1.665	1100
Site 4					
CB1290513	*Wehrlite*	0.185	0.304	1.646	1105
CB3290513	*Ol-gabbro*	0.185	0.299	1.615	1110
CB12260513	*Ol-gabbro*	0.180	0.305	1.693	1095
CB13260513	*Ol-gabbro*	0.214	0.360	1.684	1093
CB8260513	*Ol-gabbro*	0.170	0.328	1.926	1039
CB6260513	*Ol-gabbro*	0.196	0.358	1.824	1062
CB5260513	*Ol-gabbro*	0.221	0.353	1.596	1116
CB4260513	*Ol-gabbro*	0.222	0.361	1.624	1109
CB3b260513	*Ol-gabbro*	0.163	0.272	1.671	1098
CB3a260513	*Ol-gabbro*	0.209	0.335	1.602	1113
CB100	*Ol-gabbro*	0.223	0.370	1.661	1115
CB99	*Ol-gabbro*	0.227	0.396	1.741	1081

[#] Ol and cpx in disequilibrium (cf. Fig. 5e-h)

B (SE) **A (NW)**

Characteristics	***Site 1***		***Site 2***		***Site 4***		***Site 3***
Altitude	950-1200m a.s.l.		850-940m a.s.l.		660-750m a.s.l.		750-870m a.s.l.
Field work							
Structural characteristics	**Lenses and stratifications, no dynamic structure**			----	**Layered, some dynamic structures**	----	**Layered, numerous dynamic structures**
Petrology							
Dominante Paragenese	**Dunite and werhlite**			----	**Olivine gabbro**	----	**Ferrogabbro**
Geochemistry							
MgO (wt%)	**42.3**	----	**38.7**	/	**15.1**	----	**8.9**
Na_2O (wt%)	**0.14**	----	**0.16**	----	**0.98**	----	**1.65**
Eu(ppm)	**0.12**	----	**0.4**	----	**0.8**	----	**1.19**
Ni(ppm)	**2164**	----	**1716**	/	**293**	----	**154**
Sc(ppm)	**6.7**	----	**10.9**	/	**49.3**	----	**47.9**
Minerals composition							
Ol Fo (%)	**85.6**	----	**85.2**	/	**74.8**	----	**75.5**
Cpx Mg# (%)	**87.3**	----	**81.4**	----	**78.9**	----	**77.8**
Plg An (%)	**80.5**	**?**	**16.8***	**?**	**71.0**	----	**67.8**
Ox Mg# (%)	**24.9**	----	**26.4**	----	**4.7**	----	**2.9**

---- = Continuum

/ = Gap

* = Interstitial plagioclases